Year One Progress Report: Surface Chemistry of Plutonium Oxide for Waste Pretreatment

Richard E. Wilson[1], Julia Neumann[1], Srikanth Nayak[1],
Ahmet Uysal[1], Brian Powell[2], and Dawn Montgomery[2]

[1]Chemical Sciences and Engineering Division, Argonne National Laboratory
[2]Department of Environmental Engineering and Science, Clemson University

June 2025

Acknowledgments

This work was conducted at Argonne National Laboratory, operated by UChicago Argonne, LLC for the United States Department of Energy (U.S. DOE) under Contract DE-AC02-06CH11357 and supported by the U.S. DOE Office of Environmental Management through National Laboratory Program Announcement Number LAB 23-EM001 award number 277518.

Executive Summary: Project Key Findings and Impact on Acceleration of Hanford Tank Waste Clean Up Mission

This research project is focused on developing waste pretreatment strategies to reduce or eliminate the formation of transuranium wastes during tank side cesium removal operations (TSCR). This research is motivated by the observations that transuranium elements, in particular plutonium, are adsorbed to the Ionsiv ion-exchange material used for TSCR operations. This material, more generally known as crystalline silico titanate (CST) is an effective ion-exchange material for cesium removal from the high ionic strength and alkaline solutions present in the Hanford tanks.

It is observed that the primary species of plutonium present in the waste tanks is that of nanocrystalline plutonium dioxide, and these particles are known to have a unique and controllable surface chemistry that has been exploited for their separation and precipitation in our prior work.[1, 2] Using this surface chemistry, we aim to develop waste pretreatment strategies to impact the partitioning of plutonium on CST with the goal of reducing or eliminating the formation of CST TRU wastes.

Our approach encompasses study of plutonium oxide chemistry in Hanford waste tank simulants, characterization of the particle sizes, reactivity of these particles with common Hanford waste anions in alkaline conditions, study of their chemical interactions with CST and other sorbents, spectroscopic validation of the observed chemistry and modeling of the solution chemistry and adsorption properties of plutonium oxide on CST and other solid adsorbents. As part of our efforts we have leveraged the unique capabilities and infrastructure available at Argonne National Laboratory including the radiological laboratory space in the Materials Design Laboratory and have established a research program at the Advanced Photon Source for small angle X-ray scattering and X-ray reflectivity studies to advance our EM research objectives.

Our activities in Year One have validated our research hypotheses and provided significant positive guidance for making meaningful and impactful contributions to the TRU generation risks associated with TSCR operations using CST including:

- The plutonium oxide nanoparticles, synthesized by neutralization of acid solutions similar to the orginal process solutions, are stable as suspensions in the Hanford electrolyte simulants. These particles have a fundamental particle size of only a few nanometers but are susceptible to aggregation upon changing solution conditions that influences both precipitation and re-suspension properties. Importantly, dilution of concentrated electrolytes with water, and water with carbonate present, results in de-aggregation and re-suspension of particles. The implication of this observation is that tank pumping and dilution operations may result in increased plutonium concentrations in the TSCR feeds.

- The measured plutonium nanoparticle concentrations were investigated across a number of inorganic and organic anion chemistries. Our observations indicate that sulfate anions minimize the observed concentrations of suspended particles, though other strongly chelating anions, like oxalate and carbonate, result in increased plutonium nanoparticle concentrations. These observations, with those summarized above, suggest that there is a reactive particle surface that is dependent on the electrolyte chemistry and controllabe, validating our primary research hypothesis.

- Initial column investigations of Pu nanoparticle adsorption on CST demonstrated a preliminary capacity of 0.065 mg of Pu per gram of CST (4 microCi ^{239}Pu per gram CST) using Hanford tank simulants, an observation well in excess of the 100 nCi per gram regulatory limit.

- Column experiments that included a silica plug demonstrated an increased affinity for Pu to the silica over that of CST, demonstrating a proof of concept for waste pretreatment that would reduce or eliminate the adsorption of Pu on CST using sorbents with a selectivity for Pu as a pretreatment strategy. These observations motivate our continued research into Year 2 investigating the adsorption of Pu on other sorbents and the impacts of the electrolyte compositions in negating Pu partitioning to CST.

In the following report, details of our experimental efforts are outlined by task and focus. In the whole, all of these efforts are pivotal to achieving our research goals and we expect to provide actionable and practical solutions for waste pretreatment and mitigating TRU waste generation.

Table of Contents

1 Introduction & Motivation

The current flow sheet for the tank-side cesium removal (TSCR) process for use at Hanford is designed to remove radioactive cesium from the tank liquids ultimately removing ninety nine percent of the radioactivity associated with the liquid wastes resulting in a low-activity waste stream that can be treated by vitrification. Removal of the cesium is accomplished through ion-exchange of the liquids and suspended solids using crystalline silicotitanate (CST) as the exchange material. Despite the efficacy of CST for removing cesium, this material is also moderately effective at removing transuranium elements from the tank liquids, creating a risk of producing CST material that would be classified as transuranic waste (TRU), a waste form that currently does not have a path forward for disposal.

The adsorption of Pu and other transuranium isotopes on CST has been demonstrated in a publication by Campbell that analyzed the CST by digestion after contact with Hanford tank wastes from AP-107 and AW-102.[3, 4] Despite similar activities of waste feeds with respect to the Pu fractions, the lead and lag columns in the process simulation using the AP-107 wastes were either very near ca. 91 nCi per gram, or in excess, 101 nCi per gram of the TRU limit, thus creating uncertainties regarding the formation of TRU-CST wastes during TSCR operations.

This research program aims to address the risks of TRU generation during TSCR through the development of waste pretreatment strategies aimed at managing the adsorption of Pu on CST during the ion-exchange processes. Our approach is based on knowledge that;

- The plutonium speciation in the Hanford wastes is principally that of nanocrystalline PuO_2 formed as a result of process waste discharges as either solid Pu or resulting from the neutralization of acidic Pu process wastes.
- The plutonium oxide particles, typically defined as plutonium colloids or polymer have a discrete chemistry associated with their surfaces that can be tuned and manipulated to impact the partitioning of these particles.
- Waste pretreatment strategies based on the surface chemistry of the plutonium oxide particles can be developed to either reduce or eliminate the association of the plutonium oxide phases with the CST ion-exchange material.

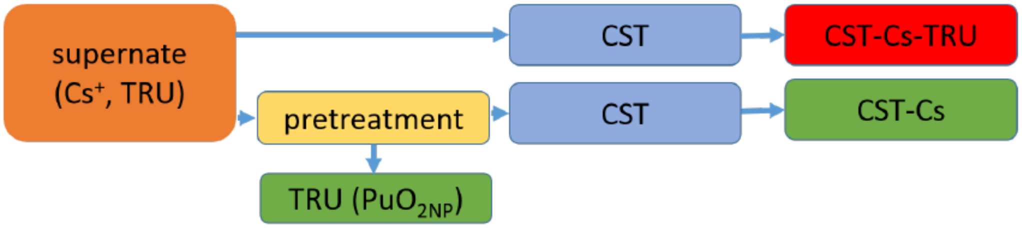

Figure 1. Simplified flow-sheet of supernate processing with CST. The current technology runs the risk and has been shown to generate TRU wastes. We propose to understand PuO2NP surface chemistry enabling pretreatment of the wastes to avoid the classification of the CST as TRU wastes.

Our proposed research and methods are based on the following hypotheses:

- $PuO_2 \cdot xH_2O$ is present as nanocrystalline PuO_2 particles that have a well-defined surface chemistry and reactivity.
- The surfaces of are: (**1**) reactive toward ligand and ion-exchange of both cations and anions, (**2**) may be manipulated to tune their overall particle charge, reactivity, and stability.
- The manipulated particle properties of will allow for their separation either by: (**1**) selective adsorption onto a membrane or filter material, and/or (**2**) tuned to be inert to surface adsorption during the CST process.
- A model of Pu behavior and partitioning based on this chemistry can be developed to inform the assessment of waste treatment options for Pu disposition.

This report summarizes our accomplishments in the first full year of this project. Described below are our observations and results that include our initial scoping experiments with surrogates Ce and U that addressed refining our experimental protocols with Pu, and our experiments investigating the chemical behavior of Pu in the high ionic strength and high alkalinity Hanford electrolytes. We have developed and applied research protocols involving laboratory

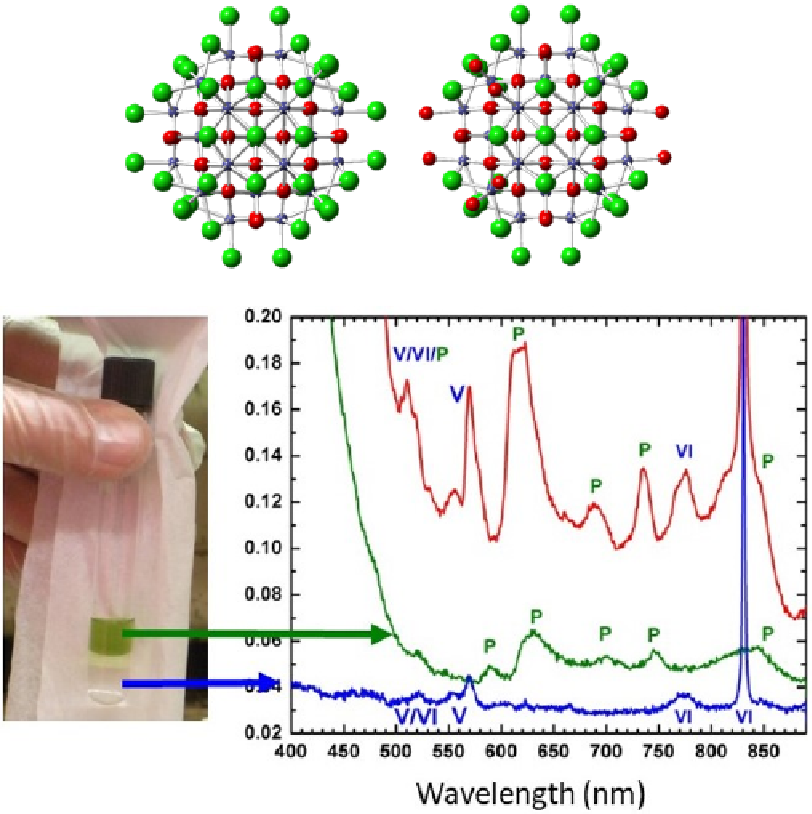

Figure 2. Structures of plutonium oxide nanoparticles isolated from aqueous solutions highlighting the different particle stoichiometries, overall particle charges, and surface stoichiometries. The cluster on the left differs from the one on the right by the surface anion and water stoichiometry, Li14Pu38O56Cl54(H2O)8 versus Li2Pu38O56Cl42(H2O)20, the lower panel highlights the effect of manipulating the surfaces of the particles to separate them from ionic plutonium species.

studies of the chemistry, electron microscopy imaging, dynamic light scattering, potentiometry, surface specific spectroscopies, and synchrotron based small angle X-ray scattering to further our research mission as originally proposed. Our research efforts continue to advance on schedule.

Significantly our results highlight the following of relevance to our mission of addressing TRU waste formation during TSCR, and the formulation of waste pretreatment strategies based on our scientific investigations:

- The plutonium oxide nanoparticles, synthesized by neutralization of acid solutions, are stable as suspensions in the Hanford electrolyte simulants. These particles have a fundamental particle size of only a few nanometers but are susceptible to aggregation upon changing solution conditions that influences both precipitation and re-suspension properties. Importantly, dilution of concentrated electrolytes with water, and water with carbonate present, results in de-aggregation and re-suspension of particles. The implication of this observation is that tank pumping and dilution operations may result in increased plutonium concentrations.

- The measured plutonium nanoparticle concentrations were investigated across a number of inorganic and organic anion chemistries. Our observations indicate that sulfate anions minimize the observed concentrations of suspended particles, though other strongly chelating anions, like oxalate and carbonate, result in increased plutonium nanoparticle concentrations. These observations, with those summarized above, suggest that there is a reactive particle surface that is dependent on the electrolyte chemistry, validating our primary research hypothesis.

- Initial column investigations of Pu nanoparticle adsorption on CST demonstrated a preliminary capacity of 0.065 mg of Pu per gram of CST (4 microCi ^{239}Pu per gram CST) using Hanford tank simulants, an observation well in excess of the 100 nCi per gram regulatory limit.
- Column experiments that included a silca plug demonstrated an increased affinity for Pu to the silica over that of CST, demonstrating a proof of concept for waste pretreatment that would reduce or eliminate the adsorption of Pu on CST using sorbents with a selectivity for Pu as a pretreatment strategy. These observations motivate our continued research into Year 2 investigating the adsorption of Pu on other sorbents and the impacts of the electrolyte compositions in negating Pu partitioning to CST.

Our research plans for the next year will focus on the adsorption of Pu to CST and other sorbents with the goal of providing both molecular level and bulk scale observations of the chemistry. Modeling efforts of the particle surfaces are ongoing as described in the subsequent sections, and our experimental data will be modeled, validated by spectroscopic observations of the chemistry, to generate the necessary parameters to evaluate pretreatment and mitigation strategies addressing the formation of TRU wastes during TSCR.

2 Surrogate Nanoparticles: Development of Synthesis Approaches and Particle Characterization in Concentrated Electrolytes

2.1 Synthesis and Characterization of CeO_2 NPs and their Reactivity in Concentrated Electrolytes

Srikanth Nayak, Richard E. Wilson

Background. Ceria nanoparticles (CeO_2 NPs) of different morphologies have been synthesized by chemical precipitation and hydrothermal methods. The morphology of the formed nanoparticles is known to be affected by the precursor salt, its concentration, pH, temperature, reaction time, and capping agents. Particle morphology can affect the surface chemistry by altering the density of surface functional groups and defects such as oxygen vacancies. Thus, characterizing the nanoparticle morphology is essential for understanding the chemical equilibria at the surface that determine the stability of nanoparticles in electrolyte solutions.

Methods. We synthesized the CeO_2 NPs by refluxing 0.1 M of ceric ammonium nitrate solution in water for 24 h. The pale orange solution turns pale yellow with an off-white precipitate. The precipitate was washed with 0.1 M HNO_3 three times and the particles were resuspended in water by ultra-sonication. The pH of the suspension was measured to be around 2.4 and Ce concentration was measured by Agilent 8900 QQQ ICP-MS. The nanoparticles were characterized by dynamic light scattering (DLS), transmission electron microscopy (TEM), and small-angle X-ray scattering (SAXS) measurements. SAXS measurements were conducted at Sector 12-ID-D at the Advanced Photon Source (APS) at ANL using an X-ray energy of 12 keV. TEM images were obtained for samples of CeO_2 NPs drop-cast on lacey carbon grids using the picoProbe at Argonne. The cerium concentration in the supernatants is a measure of particle numbers in suspension and hence of the colloidal stability. For characterization of pH-dependent colloidal stability, the CeO_2 NPs suspension pH was raised by adding aliquots of NaOH solution and the pH measured by potentiometry. For ionic-strength dependence, samples were prepared by adding a fixed amount of CeO_2 NPs to solutions of $NaNO_3$ with varying concentrations. The samples were then centrifuged, and the supernatant was digested in conc. HNO_3 for ICP-MS measurements to measure the cerium concentration in solution.

Particle Size Characterization. Hydrodynamic size measured by DLS shows that the CeO_2 NPs prepared by the reflux method have a uniform size distribution with an average hydrodynamic size of ∼9 nm (Figure 3a). The corresponding SAXS pattern in Figure 3b shows particle-like scattering with two prominent undulations. The data was fit to a model of two non-interacting spherical populations of particles. Inter-particle interactions are ignored due to the low concentration of the particles. From the model, we obtain particle sizes of $D_1 = 7.30 \pm 0.02$ nm with a log-normal size distribution ($\sigma = 0.22$, relative width of the distribution) and $D_2 = 2.32 \pm 0.08$ nm for two populations. We used the same core scattering length densities for both the particles, estimated from the density of bulk ceria. DLS is

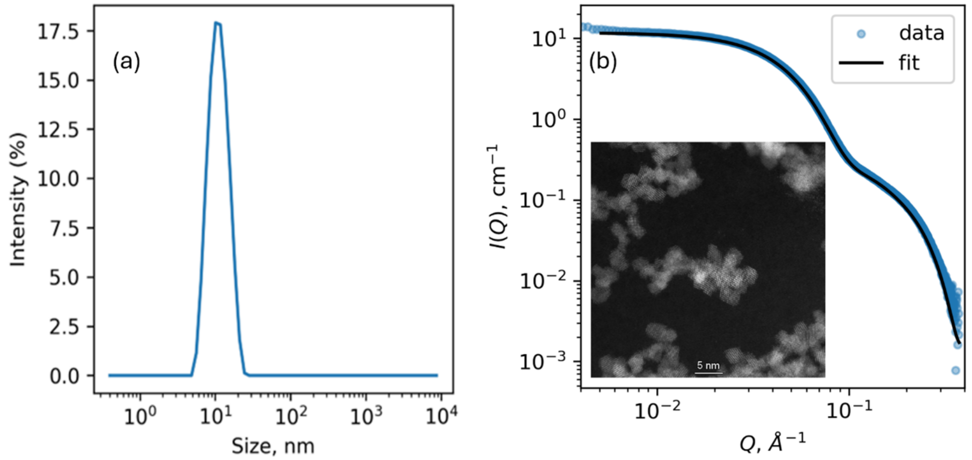

Figure 3. (a) DLS and (b) SAXS results for the CeO_2 NPs prepared by reflux method, washed and resuspended at pH=2.4. Black solid line in (b) is fit to a model of two spherical populations in the suspension. Inset to (b) shows the corresponding TEM image (courtesy of Nestor J Zaluzec, ANL) of the sample obtained by drop-casting a diluted suspension on lacey carbon grid.

disproportionately sensitive to larger particles (I $\sim$ D^6). Further, the smaller particles are likely close to the limit of detection of DLS, which explains the minor deviations between DLS and SAXS results. The TEM images in Figure 3b show aggregates with primary particles smaller than 5 nm in diameter. Based on this, the larger size particles (D_1) in SAXS are likely small aggregates of the primary particles (D_2) with a spherical shape.

Colloidal Stability in Concentrated Electrolytes. Stability of the synthesized CeO_2 NPs under varying ionic strength and pH were tested by measuring the cerium concentration in the supernatants of the nanoparticle suspension in different media. Figure 4a shows the Ce concentration in the supernatant with increasing [$NaNO_3$]. We identify a trend of decreased colloidal stability with ionic strength at [$NaNO_3$] below 2 M. Our results are consistent with predictions from DLVO theory, where the particle surface charge screening increases due to the added electrolyte, reducing inter-particle repulsion and ultimately leading to particle aggregation. Interestingly, particles appear to get resuspended above salt concentrations of 2 M, a salt concentration that exceeds the limits of DLVO theory. The phenomenon remains poorly understood; however, analogous observations have been documented for Pu(IV) colloids [5].

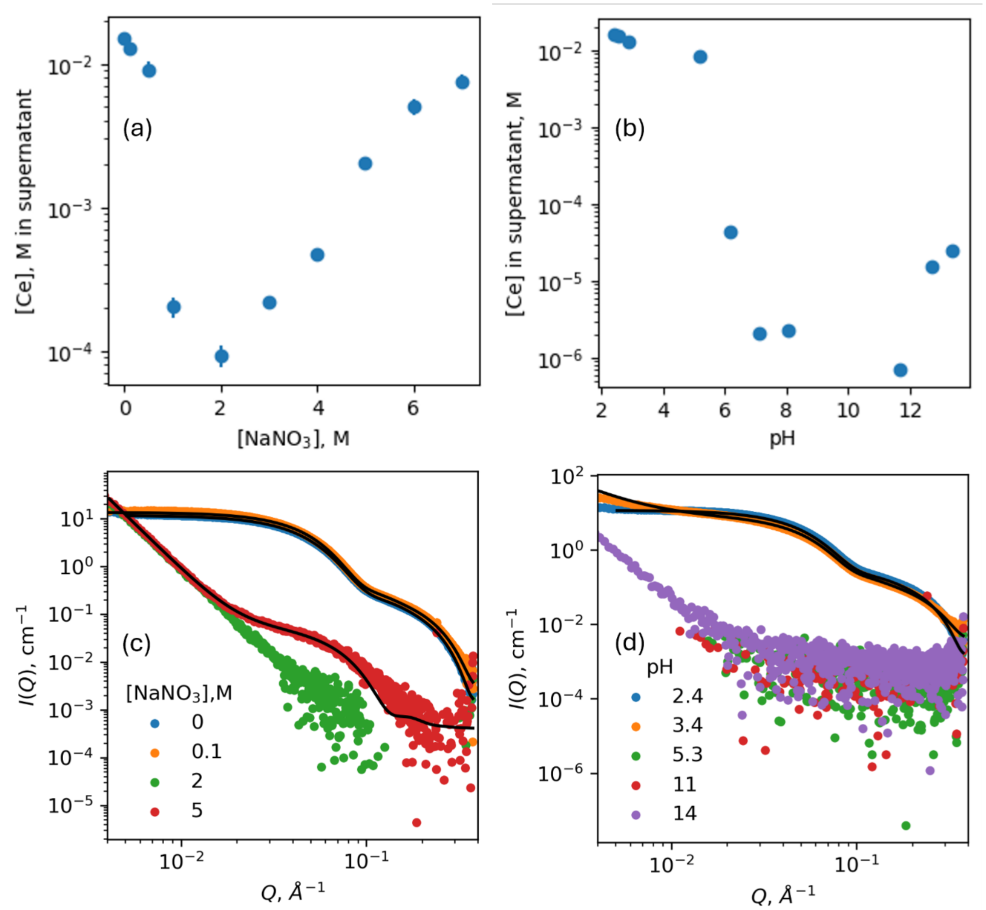

Figure 4. Cerium concentration in the supernatant of CeO_2 NP suspensions with varying (a) concentrations of $NaNO_3$ and (b) pH, obtained by ICP-MS. SAXS results for the supernatants corresponding to (a) and (b) are shown in (c) and (d), respectively. The black solid lines are fits to SAXS models described in the text. The smooth shoulders in SAXS are fit to scattering from polydisperse spheres while a power-law model is used to account for the low-Q feature due to the formation of larger aggregates.

The trend of colloidal destabilization and resuspension is observed with SAXS as well (Figure 4c). At 0 and 0.1 M of $NaNO_3$, particles are stable in suspension showing the same features as in Figure 3b. With increasing salt concentrations, power-law behavior ($\sim Q^{-4}$) in the low-Q region is observed which we attribute to very large aggregates. Since the SAXS scattering scales as R^6, even a miniscule number of aggregates in the suspension can lead to such scattering. At 2 M $NaNO_3$ only the power-law scattering is observed. At 5 M however, there is a clear particle feature which we fit to spherical particles of D=6.04±0.42 nm with log-normal size distribution (σ=0.16, relative width of the distribution) indicating that some of the smaller aggregates get resuspended at high concentrations of $NaNO_3$. We infer that the large aggregates that lead to the low-Q power law behavior are only loosely held and can be broken up by increasing salt concentration. The power-law exponent from the fit was 3.8 indicating that the aggregates are compact with smooth surfaces. The Guinier region of these aggregates is below of the Q-range measured indicating that the aggregates are larger than 100 nm.

Reactivity of CeO_2 NPs at High Alkalinity. With increasing pH, the particle stability as measured by cerium concentration decreases sharply around pH$\sim$6 and then plateaus. Notably, there is a measurable concentration of Ce ($\sim$10 μM), even at 1 M of NaOH. In SAXS measurements, the particles are well suspended at pH 2.4. At pH 3.4, a small upward tick in the scattering intensity is observed at low-Q indicating the onset of particle aggregation. At higher pH the particle features are absent and only the low-Q power-law behavior is observed, likely due to large aggregates that are still suspended. A small number of primary particles or their small aggregates that could potentially be resuspended at very alkaline conditions but they may not have enough contrast to appear in SAXS. So the SAXS results are broadly congruent with the particle stability as measured by the Ce concentration in the supernatant of the suspensions. At 0.1 M and higher $NaNO_3$ concentrations, the particle features are lost above pH = 3.4 indicating that pH and salt concentrations are interacting variables that control particle stability.

Colloidal stability is affected by the surface charge which in turn is affected by the (de)protonation of the surface, and by charge screening due to salt. At higher salt concentrations, the charge screening due to increased ion concentration in the diffuse layer can lower the energetic barrier for particle aggregation without affecting the protonation state of the surface. At pH 3.4, the particles have a lower surface charge compared to pH = 2.4 and thus a smaller concentration of $NaNO_3$ (0.1 versus 0.5 M) is sufficient to destabilize the particles. Potentiometric titrations of the CeO_2 NPs in $NaNO_3$ solutions yield a point of zero net proton charge (PZNPC) of $\sim$5.4 for salt concentrations of 10-100 mM (see Report Section 2.2 for details). In titration studies the accessible surface area for proton exchange can remain the same even after particle aggregation. Thus, while colloidal stability is a function of both pH and salt concentration, the PZNPC can remain relatively unchanged with salt concentration.

Conclusions. CeO_2 NPs were synthesized using a hydrothermal approach and characterized using techniques such as dynamic light scattering (DLS), transmission electron microscopy (TEM), and small-angle X-ray scattering (SAXS). The colloidal stability of the nanoparticles was studied under varying ionic strengths and pH conditions, including conditions relevant for the Hanford waste tanks. The observed trends in colloidal destabilization and resuspension at high ionic strengths challenge the conventional DLVO theory, suggesting new mechanisms of aggregation and disaggregation under these extreme environments that warrant further investigation. In the context of the ongoing project, the use of CeO_2 NPs as surrogates for PuO_2 NPs provided a valuable opportunity to develop workflows and sample cells for transuranium particle characterization using advanced spectroscopic and scattering techniques, as well as high-resolution imaging using electron microscopy.

2.2 Surface Charge Characterization of Bulk CeO_2 and CeO_2 NPs

Srikanth Nayak, Brian A. Powell, Dawn A. Montgomery, Richard E. Wilson

Background. Chemical complexations at the surfaces of colloidal particles significantly influence their stability by altering the surface charge and the particle-solvent interactions. Surface protonation/deprotonation and ionic adsorptions significantly affect the stability of colloidal particles suspended in electrolyte solutions. Surface complexation models (SCMs) can provide quantitative descriptions of particle surface chemistry including (de)protonation and ion-adsorption equilibria [6]. Potentiometric acid-base titrations of suspensions of colloidal particles, in the presence of various ions that can adsorb on the particle surfaces, yields necessary data for obtaining the equilibrium thermodynamic constants from SCMs.

Approach. Ceria nanoparticles (CeO_2 NPs) were obtained by refluxing 0.1 M of ceric ammonium nitrate for 24 hours and washing the resulting nanoparticle suspension successively with dilute nitric acid (see Section 2.1). The particles were then washed with water and finally resuspended in water. Potentiometric titrations were caried out in 10 mL plastic vials using a Mettler Toledo T5 Titrator. The titrand was prepared by adding an aliquot of pre-washed suspension of ceria nanoparticles to a desired electrolyte solution ($NaNO_3$ or $NaClO_4$) with known ionic strengths and acid (HNO_3 or $HClO_4$) concentrations. All the solutions were prepared with degassed water stored under nitrogen. The titration with 0.01 M NaOH was conducted under constant N_2 bubbling of the titrand. The concentration of Ce in the titrand was found to be 0.24 mM by ICP-MS. A fixed volume of the titrant was added every 10 minutes and the pH recorded. Titration was stopped when the pH read ~10. Net proton charge per mole of Ce (H) was calculated as below.

$$\Delta[H^+] = C_A - C_B - 10^{-pH} + 10^{14-pH}$$

$$\sigma_H = \frac{\Delta[H^+ \cdot F]}{m}$$

Here C_A and C_B are the concentrations of acid and base added to the titrand, F is the Faraday's constant, m is the particle concentration (in g/L or M of Ce).

Potentiometric Acid-Base Titrations. Results of the potentiometric acid-base titrations of the suspensions of ceria nanoparticles in $NaNO_3$ and $NaClO_4$ solutions are shown in Figure 5a and b. The resulting point of zero net proton charge (PZNPC) does not vary significantly with salt concentration for either $NaNO_3$ or $NaClO_4$ suspensions (Figure 5c). The anion dependence of PZNPC suggests differences in ion adsorptions in the two electrolytes. A higher number of protons need to be removed from the suspension to attain zero proton charge in the case of nitrate medium. Thus, this increase in PZNPC in nitrate suspension can be attributed to the increased adsorption of the anion in comparison to perchlorate [7]. The particle concentration at 0.24 mM of Ce is 41 mg/L (molecular weight of CeO_2 = 172.115 g/mol). The primary particles in the suspensions are < 10 nm in diameter (cf. Section 2.1, DLS and SAXS results) and consequently are expected to have a high specific surface area with large proton exchange capacity. This is reflected in the high values of σ_H away from PZNPC. Potentiometric titrations were carried out in the same electrolytes for bulk ceria suspensions as well and the resulting values are shown in Figure 5d. There is a large scatter in the values obtained from bulk ceria, possibly due to the lower surface area and proton exchange capacity. The anion dependence in PZNPC is not significant, indicating that the CeO_2 NPs and the bulk ceria powders have different surface chemistries. Similar variation in isoelectric point of ceria has been attributed to variations in material synthesis procedures [8].

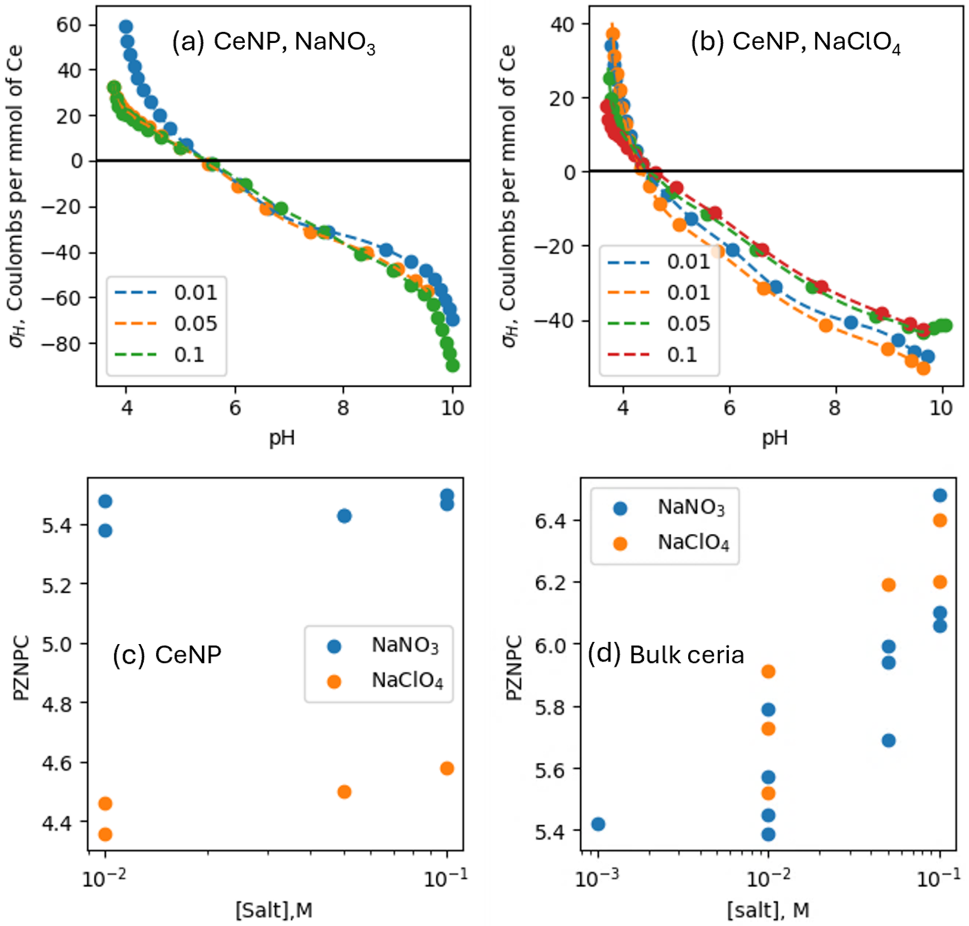

Figure 5. Net-proton charge densities on ceria nanoparticles (CeO_2 NPs) in (a) $NaNO_3$ and (b) $NaClO_4$ media. Legend entries refer to the concentration of the electrolyte in the suspensions. The solid lines through the data are guides for the eye. Variation of the point of zero net proton charge (PZNPC, σ_H=0) for (c) CeO_2 NPs and (d) bulk CeO_2 powder in $NaNO_3$ and $NaClO_4$ media.

Surface Complexation Modeling. A triple layer surface complexation model was developed to describe potentiometric titrations of bulk CeO_2 (Figure 5d, PZNPC data shown). The model adequately fit the data using only a one site protolysis model with the following reactions which include an outer sphere nitrate complex:

$\equiv CeOH + H^+ \leftrightarrows \equiv CeOH_2^+$ log K = 2.4±0.7
$\equiv CeOH \leftrightarrows \equiv CeO^- + H^+$ log K = -9.9±0.2
$\equiv CeOH + H^+ + NO_3^- \leftrightarrows \equiv CeOH_2NO_3$ log K = 2.85±3.5

where $\equiv CeOH$ represents the terminal surface of the particle. The surface site density was fixed at 28.6 sites/nm^2 based on crystallographic analysis and the surface area was fixed at 25 m^2/g. The addition of the outer sphere nitrate complex improved the quality of fit of the data but has a high level of uncertainty.

Using these same constants, the potentiometric titration of ceria nanoparticles was simulated. The surface area was estimated assuming 10 nm diameter spherical particles based on TEM imaging of the material which is equivalent to a surface area of 83 m^2/g. Other modeling approaches are being pursued now including a simpler double layer model and the more complicated charge distribution, multi-site completion model CD-MUSIC [9]. Based on the differences between the bulk CeO_2 titrations and CeO_2 NP titrations, there appear to be significant differences in surface charging behavior which are likely to also be present in comparable sized PuO_2 NPs as compared with bulk PuO_2. Thus, developing a modeling approach which can account for the differences between bulk and nanoparticulate CeO_2 will likely be transferable to PuO_2.

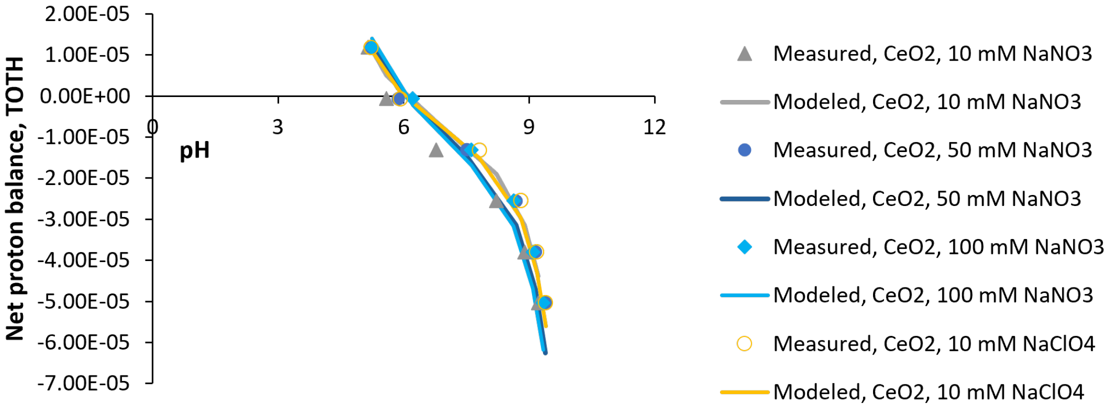

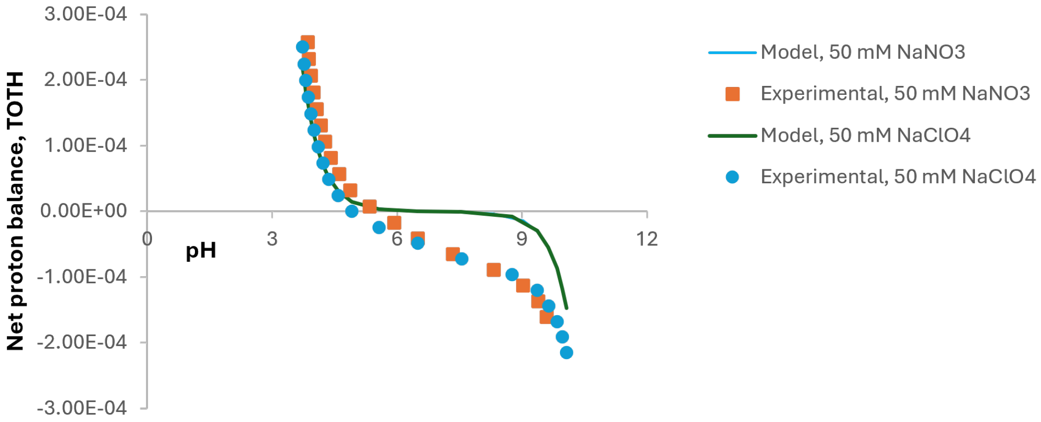

Figure 6. Top: Triple layer surface complexation model of bulk CeO_2. Bottom: Simulation of 50 mM $NaClO_4$ and 50 mM $NaNO_3$ potentiometric titration data for CeO_2 NPs using triple layer surface complexation constants determined for bulk CeO_2.

Conclusions. Our work using CeO_2 as surrogate for PuO_2 studied the surface charge properties of CeO_2 NPs and bulk CeO_2 powders using potentiometric acid-base titrations in different electrolyte solutions ($NaNO_3$ and $NaClO_4$). The titrations provide insights into surface protonation/deprotonation and ion adsorption equilibria, which are critical for understanding colloidal stability and particle-solvent interactions. The point of zero net proton charge (PZNPC) was determined for both CeO_2 NPs and bulk CeO_2, revealing significant differences in surface chemistry and charging behavior between bulk material and nanoparticles. Modeling efforts used a triple layer surface complexation model that describes the bulk CeO_2 titration data, incorporating protolysis reactions and outer sphere nitrate complexation. However, the model is inadequate to simulate CeO_2 NP behavior, highlighting the distinct surface properties of nanoparticles compared to bulk materials.

The findings underscore the importance of size-dependent changes in surface charge properties that impact the stability and reactivity of colloidal nanoparticles in electrolyte solutions. The development of a surface complexation model for CeO_2 provided an initial framework for developing experimental capabilities to study the surface charge properties of transuranium materials and surface complexation models capable of predicting the surface chemistry that can be extended to other actinide oxide systems such as PuO_2. These modeling capabilities are essential for predicting PuO_2 NP reactivity in the Hanford waste supernatants as well as the partitioning to materials used in the waste treatment processes, therefore guiding long-term waste management plans and ensuring the safe handling of nuclear waste at Hanford.

2.3 UO$_2$ Nanoparticles: Synthesis via Coulometric Titrations and Impact of Electrolytes on Particle Properties

Julia Neumann, Dawn A. Montgomery, Brian A. Powell, Richard E. Wilson

Background. Uranium dioxide (UO$_2$) is the focal point in nuclear science and materials engineering due to its critical role in the nuclear fuel cycle and environmental management. Addressing challenges such as controlling particle size, preventing agglomeration, and achieving high purity is critical for tailoring material properties to meet specifications for technological applications. Furthermore, well-controlled synthesis methods facilitate the exploration of UO$_2$ nanoparticles (NPs) in environmental systems, aiding in the development of remediation strategies for U contamination. Within the scope of the first year of the ongoing project, UO$_2$ NPs served as a less radiotoxic surrogate for transuranium NPs, enabling the establishment of workflows for particle characterization that are suitable for transuranium research.

Coulometric titration, a mild approach for inducing controlled hydrolysis of U(IV) stock solutions, has previously been reported as an effective method for synthesizing UO$_2$ NPs. However, the impact of mineral acid anions on the properties of the resulting UO$_2$ NPs remains underexplored, and comparisons between studies conducted by different groups are limited due to variations in synthesis methods and conditions. In this work, we focus on the impact of the synthesis medium (mineral acid counter-ion) on UO$_2$ NP properties as part of the initial surrogate study. Using a straightforward synthesis approach via coulometric titration under atmospheric conditions, we investigate key particle properties, including size, charge, crystallinity, and stability against oxidation, in chloride, perchlorate, and nitrate media. Additionally, we examine the role of two common ligands, sulfate and acetate, to evaluate the effects of competitive complex formation on UO$_2$ NP synthesis.

Methods. UO$_2$ NPs were synthesized coulometrically from various mineral acid solutions, including HNO$_3$, HCl, HClO$_4$, H$_2$SO$_4$, and acetic acid (HOAc). For each synthesis, the U solutions were filled into an electrochemical cell with three electrodes (working electrode, counter electrode, and pseudo reference electrode). The synthesis was performed under ambient atmospheric conditions. Initially, U^{VI} was reduced to U^{IV} at the working electrode according to the reaction:

$$UO_2^{2+} + 2e^- + 4H^+ \leftrightarrows U^{4+} + 2\,H_2O$$

A current of approximately 20-60 mA was applied to the electrochemical cell to drive the reduction. The reaction progress was monitored in operando using optical absorption spectroscopy (UV VIS). The polarization of the cell at the high potential leads to water splitting that produces OH$^-$ at the working electrode, which leads to a slow increase in pH in this half cell ($2\,H_2O + 2e^- \leftrightarrows H_2 + 2\,OH^-$), driving the hydrolysis and condensation of U^{4+} to UO$_2$ NPs:

1. Hydrolysis of U^{4+}: $U^{4+}(H_2O)_n \leftrightarrows U^{4+}(H_2O)_{n-1}(OH)^{3+} + H^+$
2. Condensation of hydrolysis products: $2\,U^{4}+(H_2O)_{n-1}(OH)^{3+} \leftrightarrows$ **...U-O-U...** + H_2O

The formed particles were characterized using dynamic light scattering (DLS), optical and vibrational spectroscopy, X-ray Diffraction (PXRD), and Transmission Electron Microscopy (TEM).

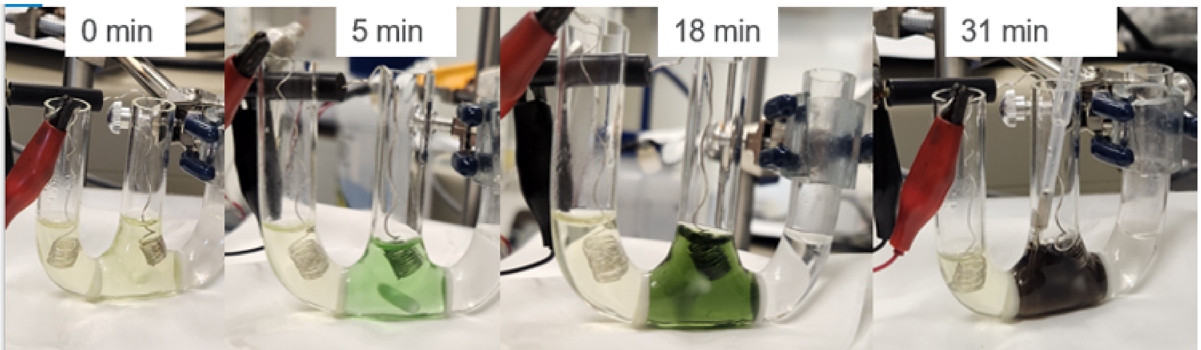

Figure 7. Typical synthesis of UO$_2$ NPs via coulometric titration, here using UO$_2$(NO$_3$)$_2$ in HNO$_3$ (yellow), leading to the reduction to U^{IV} (green solution), and formation of UO$_2$ NPs (black solution) as consequence of hydrolysis and condensation reactions.

Results. The synthesis was done first at diluted anion concentrations, typically 0.1 M UO_2^{2+} in 0.1-0.4 M mineral acid. Particle sizes were analyzed using dynamic and electrophoretic light scattering (see Table 1 for summary). Size distributions of all samples are bimodal. Based on DLS data, particles are smallest when synthesized from HNO_3, with 68% of the particles ∼8 nm. UO_2 NPs in chloride media are slightly larger with the majority (97%) having a size of ∼20 nm. In comparison, particles synthesized from perchlorate are the largest (93% of ∼55 nm) and also show the broadest size distribution, as indicated by the highest polydispersity index (PDI). Electrophoretic light scattering measures zetapotentials that serve as estimation of the particle surface charge. Particles in perchlorate show the highest zetapotential (+40.3±3.5 mV), indicating a stable colloidal suspension of positively charged UO_2 NPs. The presence of nitrate and chloride screens the surface charge of the particles to some degree, which is the reason for the lower zetapotentials, +15.8±4.4 mV and +22.1±3.9 mV for HNO_3 and HCl, respectively.

Table 1. Compilation of particle characterization using dynamic light scattering and transmission electron microscopy.

Light Scattering Results					
Mineral Acid	pH	Z_1 in nm	Z_2 in nm	PDI	Zetapotential in mV
HNO_3	1.0	8.1±0.6 (68%)	72±13 (27%)	0.40±0.01	+15.8±4.4
HCl	1.5	20±1 (97%)	>4 μm (3%)	0.18±0.03	+22.1±3.9
$HClO_4$	1.0	6.4±1.2 (7%)	55±1 (93%)	0.29±0.01	+40.3±3.5
TEM Image Analysis					
Mineral Acid	N	A in nm^2	L in nm	D in nm	AR
HNO_3	74	11.7±5.4	4.2±1.0	3.4±0.8	1.2±0.3
HCl	64	9.8±3.0	3.6±0.6	3.4±0.5	1.1±0.1
$HClO_4$	74	27±3.0	5.8±2.1	5.3±1.8	1.1±0.1

PDI: Polydispersity index, N: Particle number. A: Particle area, L: Major particle axis, D: Minor particle axis, AR: Particle Aspect ratio (=L/D), Z: Particle size.

While DLS measures particle sizes in solution, it is unable to distinguish between primary particles and agglomerates. Instead, TEM analysis allows the determination of the primary particle size. Representative TEM images of the particles synthesized from the different mineral acids are displayed in Figure 8. All samples show particles with sizes below 10 nm and crystalline cores that, according to electron diffraction patterns are UO_2 as expected, consistent with characteristic UO_2 X-ray diffraction patterns and Raman spectra of the dried UO_2 NP samples (not shown here). Statistical analysis of the TEM images shows that the primary particles in all studied mineral acids have a spherical to elliptic shape as indicated by the aspect ratio of ∼1. The primary particle size varies between 3-6 nm, and deviations between different the electrolytes are minor. Particles in chloride and nitrate have a similar size (3.4-4.2 nm), while particles in perchlorate are slightly larger (5.3-5.8 nm) and show a wider size distribution, consistent with the DLS results (Table 1).

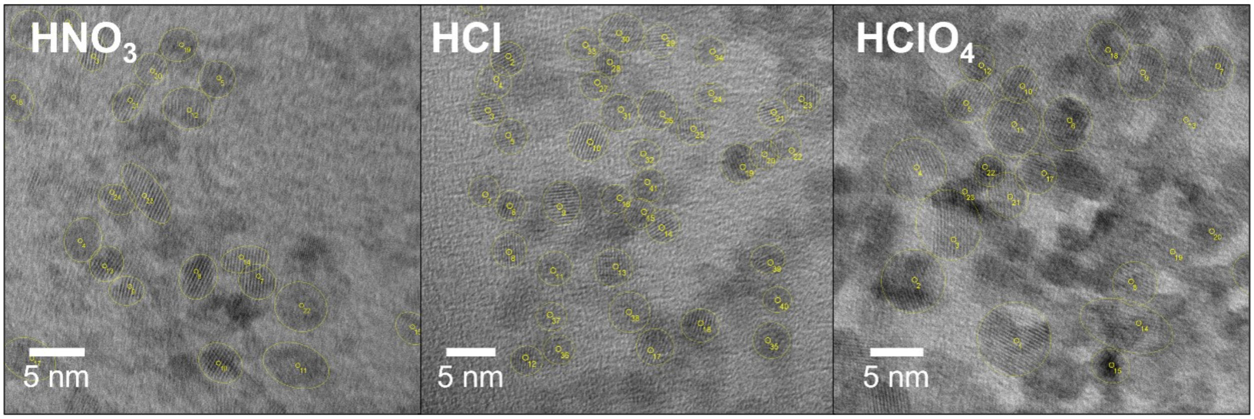

Figure 8. Transmission electron microscopy image of UO_2 NPs synthesized in HNO_3, HCl, and $HClO_4$. Yellow ellipses indicate the analysis of the grain size distribution.

Concentrated Electrolytes. An additional synthesis attempt was done in concentrated nitrate (2 M $NaNO_3$) solution. The electrochemical reduction and hydrolysis of U^{IV} is faster than in the diluted system, as indicated by a rapid increase in pH from 0.7 to 2.5 within ∼15 mins. While the solution turns dark, an immediate precipitation of solid phase occurs. The product of the reaction is a darkbrown precipitate and greyish supernatant. The supernatant contains large particles (>99% of >2μm and PDI of 0.3 based on DLS) with low zetapotentials (+6.5±1.0 mV), indicating that the high concentration of nitrate in the solution reduces the surface charge of the particles and leads to destabilization and aggregation. The precipitate was characterized using PXRD, showing the broad characteristic peaks of UO_2 (brown dataset in Figure 9, left), confirming the presence of aggregated UO_2 NPs despite the high salt content. Additional unidentified peaks in the PXRD patterns at diluted and concentrated conditions indicate the presence of other crystalline phases in the samples, likely caused by oxidation. Similarly, the dried solution of the UO_2 NPs in the diluted HNO_3 had fully oxidized upon drying (blue dataset in Figure 9, left).

For further characterization, we measured Raman spectra of the sample solution (to avoid oxidation upon sample drying) and precipitate. The data (Figure 9, right) show the characteristic T_{2g} band of UO_2 at $\sim$449-453 cm-1 that is expected to be broadened for nano-sized particles [10]. In addition to that, bands at $\sim$487-489 cm^{-1} indicate the presence of U_3O_8, oxidation product of UO_2. In the precipitate, two more bands at 329 and 423 cm^{-1} suggesting a higher amount of U_3O_8 in that phase. The two solution spectra show also intense narrow peaks at 871 cm^{-1}, indicating the presence of some U^{VI} even in solution. This is not unexpected, given the potential of nitrate to act as oxidizing agent. Experiments for high concentrations of chloride and perchlorate are ongoing and are expected to show higher stability against oxidation.

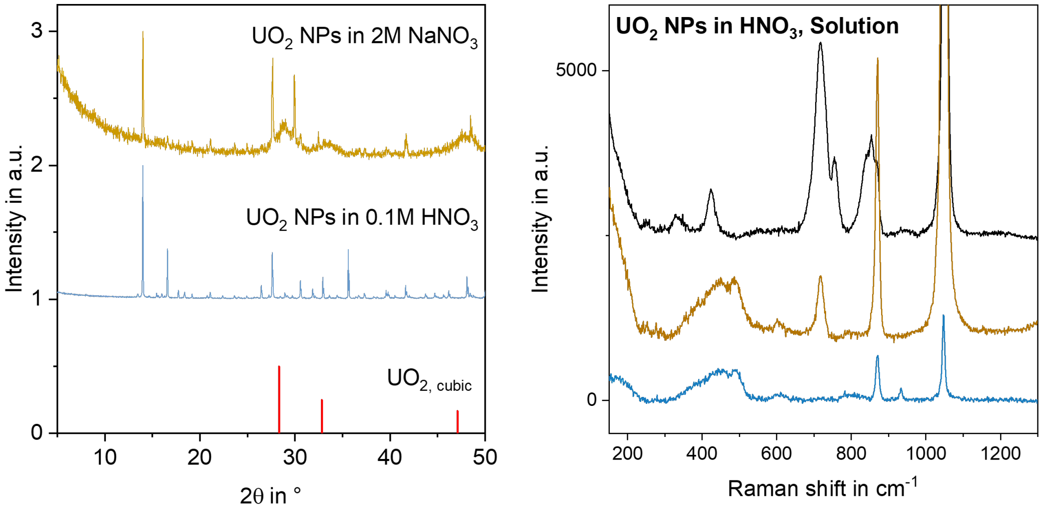

Figure 9. Left: PXRD patterns for UO_2 NPs synthesized in 0.1M HNO_3 without (blue) and with salt addition (2 M $NaNO_3$, brown). Right: Solution Raman spectra of the same samples (blue and brown), as well as solid-state Raman spectrum of the precipitate formed in the synthesis in 2 M $NaNO_3$.

Impact of Complexing Ligands. In addition to nitrate, chloride, and perchlorate, we studied the impact of three strongly complexing ligands, sulfate, acetate, trichloro acetic acid on the particle synthesis. The latter caused strong foaming in the electrochemical cell, which is why the reaction was aborted and concluded that the synthesis of the UO_2 NPs was unsuccessful. For sulfate and acetate, it was found that it depends strongly on the ligand concentration, whether or not UO_2 NPs are formed. Sulfate and acetate at 100 and 200 mM, respectively, prevent hydrolysis and particle formation, as indicated by the absence of the characteristic shoulder in the absorption spectra (Figure 10) that corresponds to the formation of $U(OH)^{3+}$ as precursor for UO_2 NPs. However, the extent of metal ion hydrolysis can be tuned by adjusting the ligand concentration. As demonstrated by the successful synthesis at lower sulfate and acetate concentrations. The progress of the reaction can be monitored spectroscopically by the absorption band that appears at $\sim$630 nm due to the hydrolysis of U^{IV}. At 5 and 100 mM sulfate and acetate, respectively, sufficient amounts of free U^{IV} are present in solution to undergo hydrolysis and start the condensation reaction, leading to successful UO_2 NP synthesis.

The synthesis in sulfate leads to a black precipitate, similar to the observation in concentrated $NaNO_3$. This is likely due to adsorption of sulfate to the particle surface, compensating the surface charge and aggregating the formed particles immediately. Characterization of the precipitate is ongoing. UO_2 NPs synthesized in the presence of acetate (final pH 3) have a bimodal particle size distribution with 90% of the NPs being 13±6 nm and a minor fraction (10%) $\sim$450 nm and show a zetapotential of +20.3±4.9 mV. In comparison to the particles synthesized in diluted HNO_3, the NPs are slightly larger yet more homogeneous in size and have a higher surface charge, indicating the colloidal suspension of particles in acetate should be more stable against sedimentation. This is consistent with the observation that this sample was present as a stable colloidal suspension, while particles in diluted HNO_3 aggregated to a black precipitate when the pH was increased to pH>3.

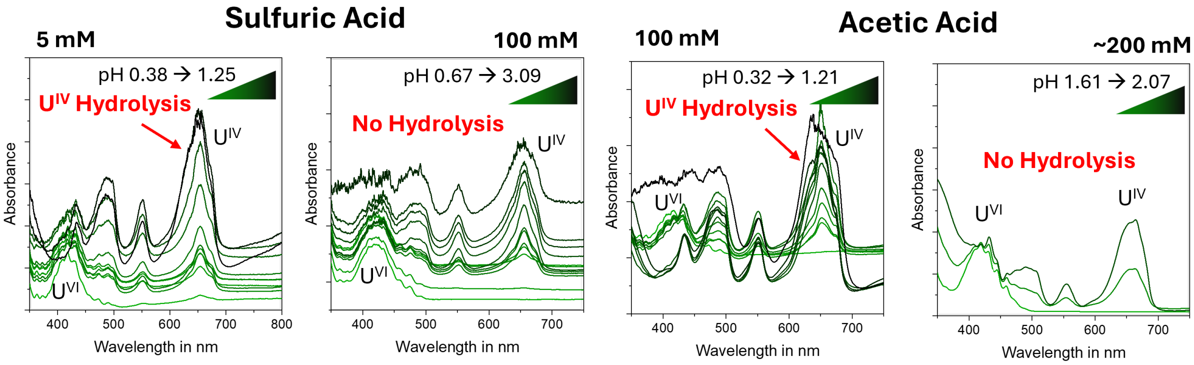

Figure 10. UV Visible absorption spectra tracking the reaction progress of U^{VI} reduction, complexation, and hydrolysis. The most characteristic absorption bands of U^{IV} and U^{VI} are marked. Importantly, a shoulder at 636 nm indicates the formation of $\mathrm{U(OH)}^{3+}$ that serves as precursor for condensation reactions that lead to the formation of UO_2 NPs.

Conclusions. Overall, this work demonstrated the capability to synthesize UO_2 NPs from different mineral acid solutions through coulometric titrations under ambient conditions and in the absence of capping agents or hydrothermal conditions. In all cases, the primary particles have the expected UO_2 crystal structure and are 3-5 nm large as observed by TEM. Parameters like solution pH and salt concentrations largely control the resulting aggregate size that is comprised of the smaller primary crystallites. The particle surface charge at acidic pH is positive as indicated by electrophoretic light scattering measurements. The differences in particle properties synthesized in different mineral acids are minor. The presence of ligands, i.e., sulfate and acetate, influence particle formation mainly through a shift in the aqueous speciation by metal complexation. As expected, particle formation depends strongly on the interplay of metal ligand complex formation and metal hydrolysis.

3 Synthesis of PuO_2 NPs in different Mineral Acids

Julia Neumann, Richard E. Wilson

Background. The formation of plutonium dioxide nanoparticles, PuO_2 NPs, in the Hanford waste tanks is a result of various chemical processes that were employed for plutonium production and separation. Understanding the chemical properties of particles synthesized from different media is important to understand their chemical reactivity within the waste streams, i.e., colloidal stability in tank waste supernates and sludges, and interactions of particles at solid-liquid interfaces such as tank and pipe walls, as well as ion exchange materials. Therefore, the first part of this project explores the impact of common anions known to be present in the waste streams on the formation of PuO_2 NPs and their particle properties.

Methods. An established way of synthesizing PuO_2 NPs is the hydrolytic approach. In this process, fresh plutonium hydroxide ($Pu(OH)_4$) precipitate is first prepared and thoroughly washed with water until the supernatant becomes neutral, ensuring the removal of excess ions and impurities. Following this, a small volume (5–10 mL) of diluted mineral acid (0.05 M concentration) is introduced to the washed precipitate. The formation of the colloid occurs through the following chemical reactions:

1. Dissolution of $Pu(OH)_4$: $Pu(OH)_4 \leftrightarrows Pu^{4+} + 4\ OH^-$, $\log K_{sp}=-58.7\pm0.9$ [11]
2. Hydrolysis of Pu^{4+}: $Pu(H_2O)_n{}^{4+} \leftrightarrows Pu(H_2O)_{n-1}(OH)^{3+} + H^+$, $\log_{10}K = -2.3\pm0.4$
3. Condensation of hydrolysis products: $2\ Pu^4{+}(H_2O)_{n-1}(OH)^{3+} \leftrightarrows$ **...Pu-O-Pu...** + H_2O

The acids used in this study include nitric acid (HNO_3), hydrochloric acid (HCl), and perchloric acid ($HClO_4$). The acidified mixture is then subjected to rigorous stirring to promote uniform interaction between the acid and the precipitate. After 24 hours, the first batch of PuO_2 NPs is collected by centrifugation. The resulting supernatant exhibits a distinct emerald-green color, which is characteristic of the presence of PuO_2 NPs in solution. The mineral acid anion impact the equlibria that lead to the NP formation mainly through complex formation, which should be negligible in perchlorate but noteworthy for chloride and nitrate media based on the complex formation constants [12]:

$Pu^{4+} + Cl^- \leftrightarrows PuCl^{3+}$, $\log_{10}K = 1.8\pm0.3$
$Pu^{4+} + NO_3^- \leftrightarrows PuNO_3^{3+}$, $\log_{10}K = 1.95\pm0.15$

The PuO_2 NPs synthesized from the different mineral acids were systematically characterized to evaluate their physical and chemical properties. Key parameters such as particle size, crystallinity, and spectroscopic features were analyzed to understand the influence of the synthesis medium on nanoparticle formation. Additionally, the aging behavior of the particles was monitored over time to assess their stability and evolution in different chemical environments. While these experiments are still ongoing, the data collected thus far provide valuable insights into the early-stage differences and long-term convergence of particle properties.

Particle Size Distributions. Initial observations revealed significant differences in particle size and size distribution during the first few days of synthesis, depending on the acid used. Specifically, nanoparticles formed in perchlorate media exhibited larger initial particle sizes and broader size distributions compared to those synthesized in chloride and nitrate media (Table 2). This suggests that perchlorate ions may influence the nucleation and growth processes differently, potentially due to differences in complexation behavior between the anions. However, after approximately one week, the particle properties across all synthesis media converged to similar values. The average particle size stabilized in the range of 90–100 nm, with polydispersity indices (PDIs) of roughly 0.2. This PDI value indicates a moderately polydisperse size distribution, which is predominantly monomodal. Dynamic light scattering (DLS) measurements (Figure 11) further confirmed that more than 90 % of the particles fell within the size range of 120±60 nm, demonstrating a consistent and reproducible particle size distribution across all media.

Particle Surface Charge. Electrophoretic light scattering experiments were conducted that measure zetapotentials, serving as proxy for the particle surface charge. The zeta potential is a critical parameter in colloidal science, as it provides insights into the stability of colloidal suspensions and the interactions between nanoparticles and their surrounding environment. Higher magnitudes of zeta potential (either positive or negative) typically indicate stronger electrostatic repulsion between particles, reducing the likelihood of aggregation and ensuring colloidal stability. Synthesized PuO_2 NPs in HNO_3 and HCl had comparable zeta potentials of +28.2±3.9 mV and +30.25±3.7 mV, respectively (values averaged over multiple syntheses batches and measurements). These values suggest that the nanoparticles formed

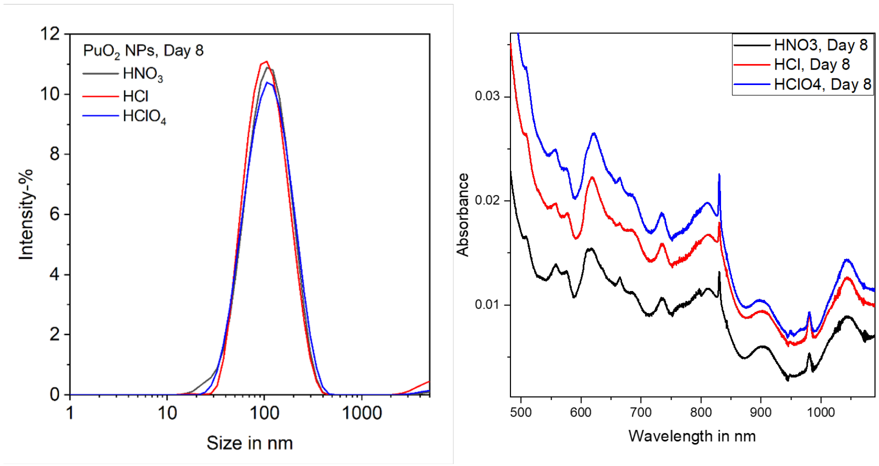

Figure 11. Particle size distribution (left) and optical spectra (right), confirming the successful synthesis of PuO_2 NPs.

in these media exhibit a stable colloidal suspension. The positive zeta potential indicates that the surface of the PuO_2 NPs carries a net positive charge, likely due to the protonation of surface hydroxyl groups ($Pu\text{-}OH_2^+$) under acidic conditions. Interestingly, PuO_2 NPs in $HClO_4$ had a slightly higher zetapotential of 38.7±1.9 mV. This difference in zeta potential magnitude can be attributed to the nature of the anions present in the synthesis medium and their interactions with the nanoparticle surface. Perchlorate is known to be a non-interacting ligand, meaning it does not strongly associate with or screen the positively charged surface of PuO_2 NPs. As a result, the surface charge remains largely uncompensated, leading to the observed higher zeta potential magnitude. In contrast, chloride and nitrate are weakly complexing ligands that exhibit some degree of interaction with the nanoparticle surface. These anions are likely attracted to the positively charged surface through electrostatic forces, resulting in partial charge compensation. This interaction reduces the magnitude of the zeta potential compared to perchlorate. While these ligands are not strong enough to form covalent bonds or significantly alter the surface chemistry of the nanoparticles, their presence influences the electrostatic environment near the particle surface. The observed differences in zeta potential values highlight the role of anion chemistry in modulating the surface properties of PuO_2 NPs.

Formation Kinetics. Differences in the reaction kinetics of PuO_2 NP formation were observed across the different synthesis media, highlighting the influence of anion chemistry on the nucleation and growth processes. Specifically, particle formation in perchlorate media was initially slower compared to chloride and nitrate media. This slower initial rate may be attributed to the non-interacting nature of perchlorate ions, which do not strongly associate with the precursor species or influence the nucleation process. In contrast, chloride and nitrate ions, as weakly complexing ligands, may facilitate nucleation through electrostatic interactions or partial stabilization of intermediate species, leading to

Table 2. Summary of particle properties for PuO_2 NPs synthesized in HNO_3, HCl, and $HClO_4$.

	[Pu] in mM	pH	Z_{Ave} in nm	PDI	Z_1 in nm	Fraction in %
HNO_3						
Day 1	0.30	1.81	131	0.38(3)	179(17)	93.5
Day 3	0.41	1.80	104	0.30(4)	140(16)	97.5
Day 8	**0.74**	**1.80**	**94**	**0.21(1)**	**120(4)**	**99.4**
HCl						
Day 1	0.22	1.81	115	0.36(2)	151(8)	94.0
Day 3	0.56	1.76	130	0.36(1)	158(13)	91.6
Day 8	**0.84**	**1.95**	**96**	**0.22(1)**	**117(56)**	**98.2**
$HClO_4$						
Day 1	0.10	1.77	192	0.49(7)	252(100)	80.8
Day 3	0.44	1.73	90	0.24(3)	108(5)	97.6
Day 8	**0.98**	**1.89**	**97**	**0.21(1)**	**124(65)**	**99.5**

faster initial particle formation. Interestingly, after the first few days of synthesis, the reaction kinetics diverged further. Particle formation in chloride media accelerated significantly, surpassing the rates observed in nitrate and perchlorate media, which remained comparable to one another (Figure 12). This acceleration in chloride media could be due to the stronger electrostatic interactions between chloride ions and the positively charged Pu-containing precursors, which may promote particle growth and aggregation. Alternatively, chloride ions may influence the solubility or reactivity of intermediate species, thereby enhancing the overall rate of particle formation. To better understand these kinetic differences, samples were collected during the synthesis process for advanced characterization. Transmission electron microscopy (TEM) imaging will be performed to examine the morphology and size evolution of the nanoparticles at different stages of synthesis. Additionally, X-ray Photoelectron Spectroscopy (XPS) will be employed to analyze the surface chemistry of the particles, providing insights into the role of anions in modulating surface properties. The samples were synthesized at ANL and are currently prepared for shipping to Clemson University for further analysis.

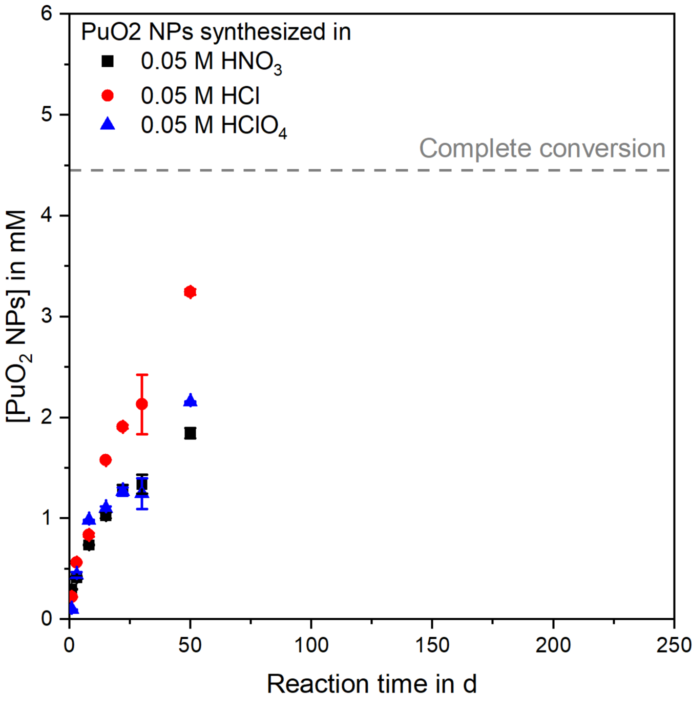

Figure 12. Left: Kinetics experiment of formation of PuO_2 NPs in diluted mineral acids of different composition. Experiments ongoing.

Outlook. In the next phase of this study, synthesis batches will be set up to investigate the impact of concentrated salts relevant to the Hanford waste environment on the properties of PuO_2 NPs. The Hanford waste tanks contain a complex mixture of salts, including high concentrations of nitrate, chloride, sulfate, and other anions, which may significantly influence nanoparticle formation, stability, and aggregation behavior. By systematically varying the concentration and composition of these salts during synthesis, we aim to better understand how the chemical environment of the waste tanks affects the physicochemical properties of the PuO_2 NPs.

4 Surface Complexation and Reactivity of PuO_2 NPs with Supernate Simulants: Influences of Electrolyte Anions

4.1 Reactivity of PuO_2 NPs in Concentrated Electrolytes

The following section is part of an article published in the Conference Proceedings of Waste Management Symposia 2025:

J. Neumann, B.A. Powell, D.A. Montgomery, R.E. Wilson, (2025). Colloidal behavior of plutonium oxide in concentrated electrolyte solutions. Waste Management Symposia 2025: Conference Proceedings, Article ID: 25207. https://www.osti.gov/biblio/2565226

Background. Fundamental research underpinning the behavior of PuO_2 NPs under conditions not only relevant to the Hanford tank waste but at high ionic strength in general is needed to reliably predict the chemical reactivity of PuO_2 NPs and develop engineering solutions to safely and efficiently process high-level radioactive waste into forms suitable for long-term storage. Overall, the available data on PuO_2 NP stability in concentrated electrolytes is scarce, especially for electrolytes other than nitrate and particularly within the extreme electrolyte concentrations of the high-level waste tanks. Therefore, in this work we aim for systematic characterization of stability ranges of PuO_2 NPs in highly concentrated electrolyte solutions of different anion composition (NO_3^-, Cl^-, ClO_4^-, SO_4^{2-}, $C_2O_4^{2-}$, CO_3^{2-}) at concentrations of up to 5 M, in both acidic and alkaline pH regimes.

Methods. Aliquots of the PuO_2 NP suspension were used as described in Section 3 of this report, and exposed to high electrolyte concentrations (0.05–5 M) by adding different amounts of the salts $NaClO_4$, NaCl, $NaNO_3$, Na_2SO_4, or $Na_2C_2O_4$ to the sample solution (Figure 13). After equilibration, the samples were allowed to settle for 1h, after which aliquots were taken for measurement of the [Pu] in solution using LSC. To study the reactivity of PuO_2 NP under alkaline conditions, the pH of the Pu suspension was raised using NaOH, which resulted in coagulation of the PuO_2 NPs. The coagulate was exposed to concentrated electrolyte solutions ($NaClO_4$, NaCl, $NaNO_3$, Na_2SO_4, or $Na_2C_2O_4$) at alkaline pH to study whether these electrolytes facilitated resuspension of the particles. One additional sample was set up in which PuO_2 coagulate was diluted with DIW to simulate the addition of water to waste sludges.

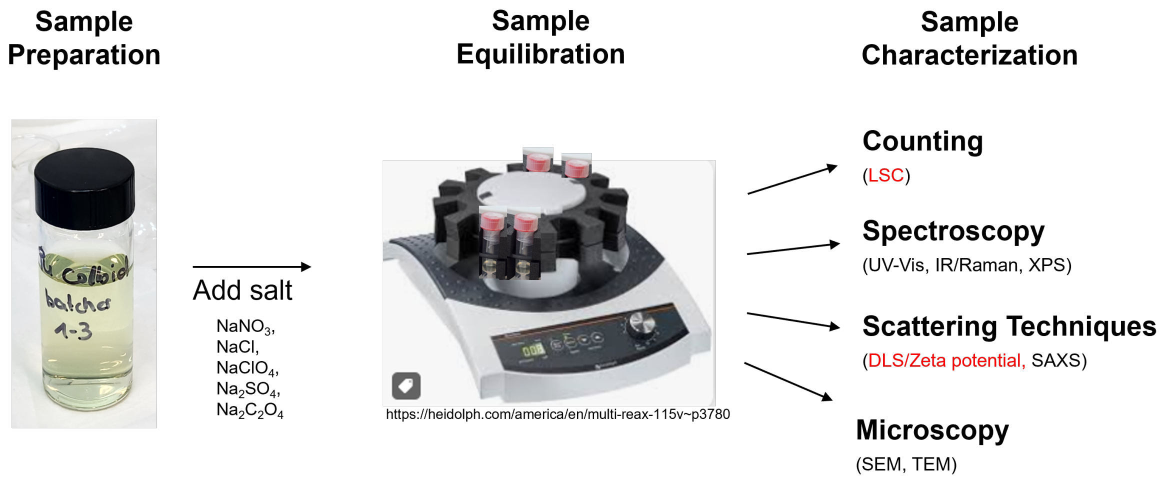

Figure 13. Overview of the experimental approach to study the reactivity of PuO_2 NPs in concentrated electrolyte solutions. Data from characterization techniques discussed in this section are marked red. Data from spectroscopic studies is shown in Report Section 5. Microscopy and SAXS experiments are currently pending.

PuO_2 NPs in Concentrated Electrolytes in Acidic pH Regime. In the initial work, we focused on high salt levels on the acidic pH side to study the response of the stable colloidal suspension to high concentrations of various salts. The data show major differences in the impact of the different electrolytes on aggregation and sedimentation reactivity. Specifically, nitrate stabilizes the suspension over the entire concentration range more than any other investigated electrolyte, as characterized by a nearly constant [Pu] and decrease in average particle size with increasing electrolyte concentration (Figure 14). Addition of large amounts of perchlorate and chloride cause aggregation into larger particles, leading to a slight decrease in [Pu] at higher salt concentrations. Sulfate interacts strongly with the PuO_2 NP

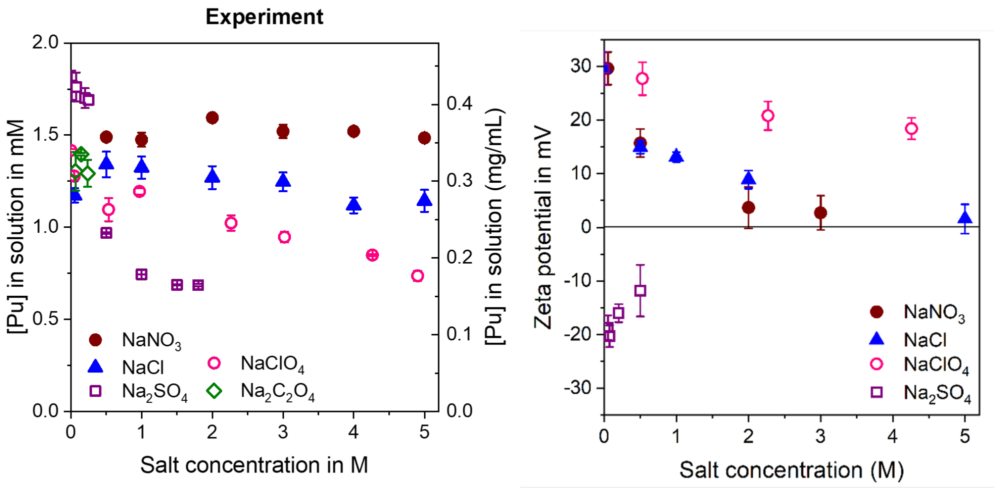

Figure 14. Left: Changes in [Pu] in solution as function of salt concentration for different electrolytes as experimentally determined. Right: Changes in zeta potential as function of salt concentrations at acidic pH values.

surface, reverses the particle charge and precipitates the particles efficiently, even at low concentrations (∼0.5 M), as indicated by negative zetapotentials 14, right). No other investigated electrolyte shows this effect. High concentrations of nitrate, chloride, and perchlorate merely lead to charge screening, resulting in a decrease of the magnitude of the zetapotential; however, the particles remain positively charged. Another interesting electrolyte that was studied is oxalate. Addition of moderate amounts of Na oxalate cause the pH to increase while the [Pu] remains unchanged up pH ∼4.8. The mechanism responsible for these elevated [Pu] at near neutral pH were studied spectroscopically (cf. Report Section 5 for more details) but will need further exploration in the future.

Impact of pH on Colloidal Stability of PuO_2 NPs. The stability of PuO_2 NP suspensions is strongly influenced by the pH and ionic strength of the surrounding medium. While the PuO_2 NP suspensions are mostly stable at acidic pH (pH<4), they are destabilized at higher pH due to a decrease in particle charge. This destabilization leads to a significant decrease in the [Pu] in solution. [Pu] are found to decrease from ∼1 mM to ∼0.01 mM for pH>4.5, and remain at this level even under strongly alkaline conditions (green data in Figure 15).

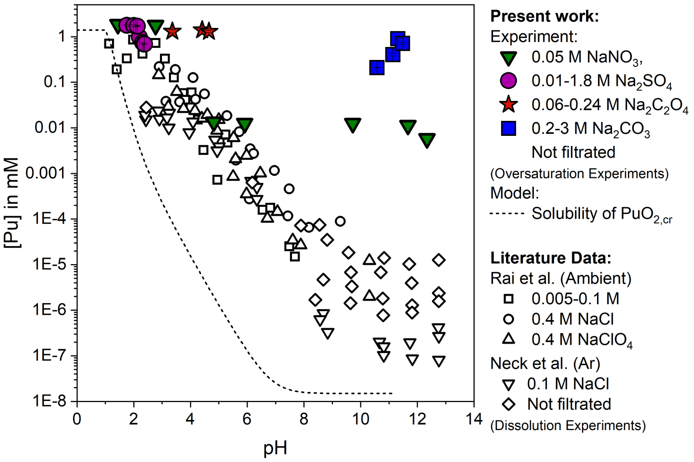

Figure 15. Impact of investigated electrolytes on measured [Pu] in solution and comparison to experimental Pu solubility data reported by Rai and Neck et al. [13].

The observed decrease in [Pu] at high alkalinity is attributed to the aggregation and precipitation of PuO_2 NPs, driven by reduced electrostatic repulsion between particles as the surface charge diminishes. However, the measured [Pu] in highly alkaline solutions during our neutralization experiments, where oversaturation of Pu in solution occurs, are found to be 2–5 orders of magnitude higher than the solubility of PuO_2 determined through dissolution experiments [13]. This discrepancy highlights the complicated impact of PuO_2 NPs on [Pu] in alkaline environments, where colloidal stability and solubility are influenced by factors beyond simple equilibrium thermodynamics. Importantly, the measured [Pu] in highly alkaline solutions is strongly dependent on experimental conditions, including sample preparation methods and whether filtration or (ultra)centrifugation was applied. For example, filtration or centrifugation can remove larger aggregates or colloidal particles, significantly altering the apparent [Pu] in solution. To ensure the relevance of our experiments to the conditions observed in Hanford waste tanks, we refrained from filtration and centrifugation except when necessary to characterize particle sizes. This approach ensures that our results reflect the behavior of PuO_2 NPs under realistic waste tank conditions. Notably, all reported [Pu] concentrations in alkaline solutions are several orders of magnitude higher than the solubility of crystalline PuO_2 predicted by thermodynamic models, represented by the dashed line in Figure 15. The modeling aspect of this work is discussed further in Report Section 4.2). The discrepancies evident in Figure 15 underscore the importance of considering non-equilibrium processes, such as colloidal stabilization and aggregation when interpreting Pu behavior in alkaline environments.

PuO_2 NPs in Concentrated Electrolytes in Alkaline pH Regime. The PuO_2 NP solution at pH 13 was used to test the impact of various electrolytes on the colloidal stability. The results are shown in Figure 16. The [Pu] in the starting solution (containing 0.05M nitrate from the particle synthesis) was 0.06 μM. Upon addition of $NaClO_4$, the [Pu] decreases further and reaches the detection limit of LSC (here 0.01 μM) at 5 M $NaClO_4$. Nitrate, chloride, and

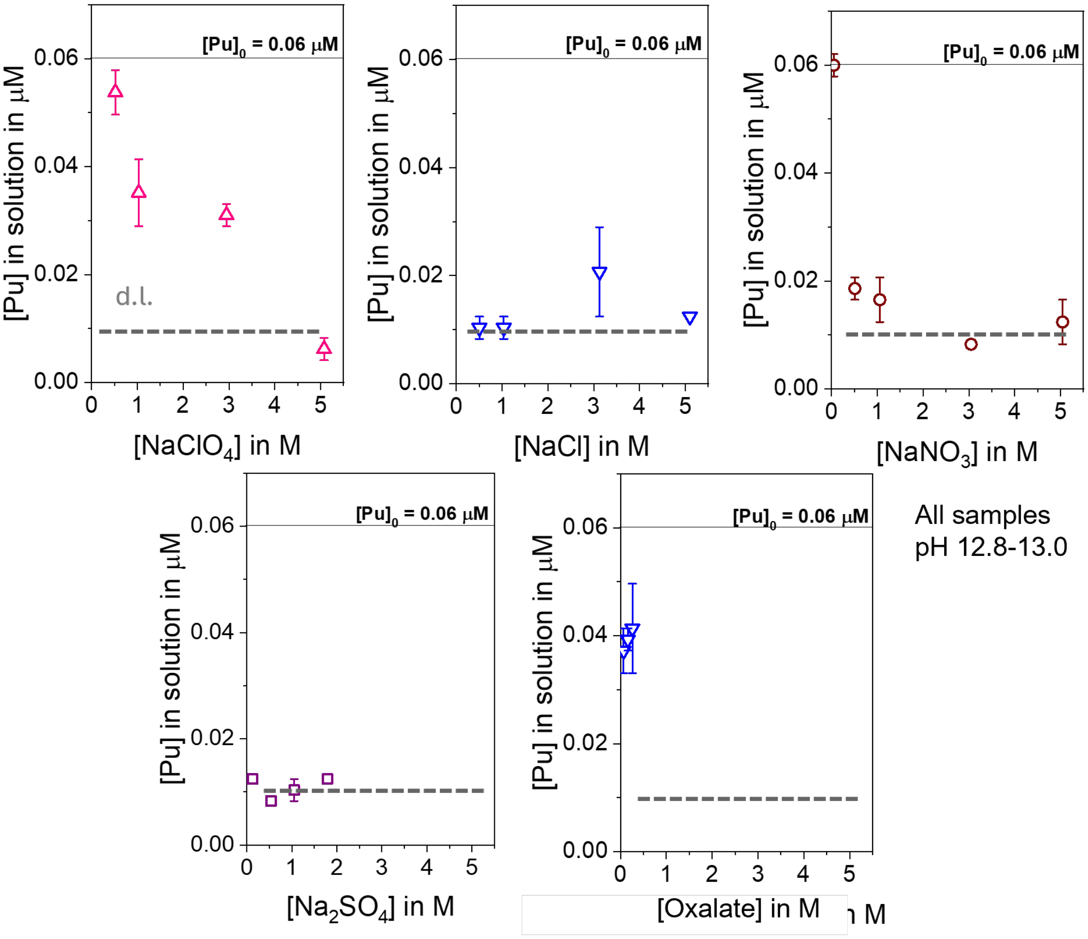

Figure 16. Impact of increasing salt concentrations on PuO_2 NP colloidal stability. Grey dashed lines mark the detection limit of LSC.

sulfate, which are all stronger complexing ligands than perchlorate, lead to efficient particle aggregation for >1M salt concentration, as indicated by [Pu] that are in no case above the LSC detection limit. Interestingly, oxalate is the only ligand under alkaline conditions that reduces the [Pu] in solution only slightly to ∼0.04 μM. Additional experiments using a Pu isotope with a higher specific activity, such as Pu-238 and Pu-239, would allow a lower LSC detection limit and could provide further insights in differences in the reactivity of chloride, nitrate, and sulfate media under highly alkaline conditions. Unfortunately, due to the low particle concentrations in solution, characterization of the particle sizes and charges using DLS, spectroscopic and scattering tools is impossible. Samples were prepared for high-resolution imaging and are currently prepared for shipping to Clemson University.

Interestingly, the aggregation and sedimentation reactivity upon neutralization described in the previous section is prevented up to very high alkalinity (pH∼12) by the presence of moderate amounts (> 0.25 M) of carbonate as a ligand that appears to strongly interact with the PuO_2 NP surface, leading to extremely stable colloidal suspensions even at alkaline pH (Figure 17, bottom). Here, at >1.5 M Na_2CO_3 0.7-0.9 mM Pu can be found in solution. Surprisingly, centrifugation of the carbonate samples does not lead to a significant decrease in [Pu] in solution, underlining the high stability of the colloidal suspension and presence of small particles in carbonate media. The polydispersity of the samples increases significantly, making the carbonate samples unsuitable for DLS measurements. An attempt to measure the zeta potential of the particles yields values of -5.4±2.8 and -2.4±2.6 mV at 1.7 and 2.9 M Na_2CO_3, respectively. While the magnitude of these zetapotential values can be questioned because of the high heterogeneity of the sample and the high ionic strength conditions, the fact that the particle charge is negative in the presence of carbonate seems reasonable, either due to a high number of deprotonated surface sites at high pH and/or inner-sphere coordination of the (bi)carbonate ions to the PuO_2 NP surface, consistent with the known high affinity of carbonate for Pu^{IV} [12].

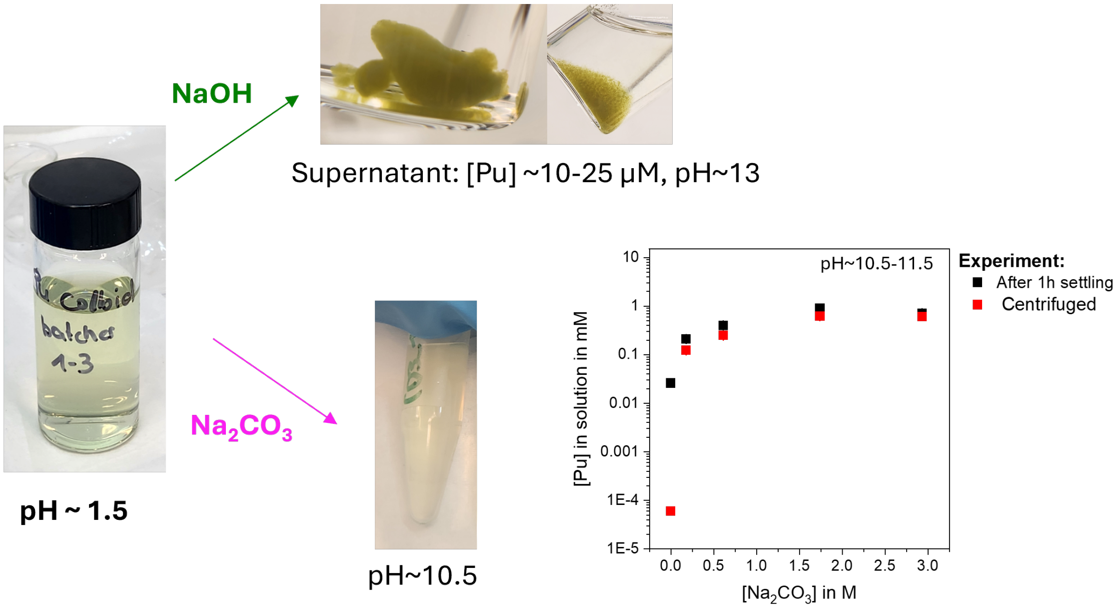

Figure 17. Left: [Pu] in solution for Pu colloid reacted with Na2CO3 and comparison to the predicted [Pu] by the thermodynamic model, in which the pH values were constraint by the experimentally measured valued. The total Pu concentration in the model was 1.3 mM. The 0 M carbonate sample corresponds to Pu colloid in NaOH at pH 13.8.

Reactivity of PuO_2 NP Coagulates with Diluted and Concentrated Electrolytes in Alkaline Media. Lastly, a suspension containing the PuO_2 NP coagulate prepared by NaOH addition was exposed to different electrolyte solutions at high pH and high salinity to study the reversibility of aggregation at high ionic strength. The [Pu] of the samples was measured first after 1.5 h of settling, as shown in black symbols in Figure 18. [Pu] are low in the diluted electrolytes, i.e., [Pu] ∼0.05 mM in 0.05 M $NaNO_3$ and 0.4 M Na_2SO_4, and slightly elevated in the other studied electrolytes (0.2–0.32 mM Pu), possibly caused simply by a slower settling velocity in electrolytes that have a higher viscosity. One interesting additional dataset was acquired for the PuO_2 coagulate resuspended in deionized water. The pH value sample is slightly lower (12.3) than in the supernatant but still comparable to the other samples in this series. The dilution with deionized water is the more efficient in resuspending the PuO_2 NPs into (sub)-micrometer-sized particles that do not settle within 1.5 h ([Pu] = 0.27 mM) than any other electrolyte solution, and ∼7% of these particles are resistant to centrifugation, causing [Pu] in solution to increase up to ∼20 μM after centrifugation. Overall, the presented results show that high ionic strength electrolytes are not very efficient in de-aggregating PuO_2 coagulate. However, dilution with low ionic strength solutions, high pH solutions containing moderate amounts (>0.25 M) of carbonate, or simple dilution with DIW are very effective to de-aggregate PuO_2 NPs and result in significant increase of [Pu] in solution.

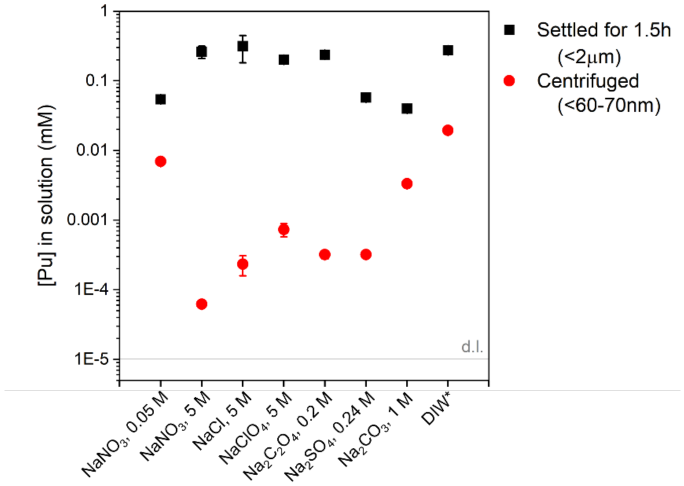

Figure 18. [Pu] in solution after reacting the PuO_2 NP coagulate with electrolyte solutions. pH

Conclusions. In the present work, we aimed for a systematic study of the impact of high concentrations of different electrolytes on the colloidal stability of freshly synthesized PuO_2 NP in solution. The data show major differences in the impact of the different electrolytes on aggregation and sedimentation reactivity. Specifically, in the acidic pH regime, nitrate stabilizes the suspension over the entire concentration range more than any other investigated electrolyte, as characterized by a nearly constant [Pu] and decrease in average particle size with increasing electrolyte concentration. Addition of large amounts of perchlorate and chloride cause aggregation into larger particles, leading to a slight decrease in [Pu] at higher salt concentrations. Sulfate interacts strongly with the PuO_2 NP surface, reverses the particle charge and precipitates the particles efficiently, even at low concentrations (∼0.5 M). Addition of moderate amounts of oxalate cause a high [Pu] even at pH ∼4.8. The mechanism responsible for these elevated [Pu] will need further exploration in the future. While the PuO_2 NP suspensions are mostly stable in dilute nitrate media for pH<4, they are destabilized at higher pH by a decrease in particle charge, leading to efficient decrease in [Pu] at alkaline pH. This aggregation and sedimentation reactivity at pH>4 is prevented up to very high alkalinity (pH 12) by the presence of moderate amounts (>0.25 M) of carbonate as a ligand that appears to strongly interact with the PuO_2 NP surface, leading to extremely stable colloidal suspensions even at alkaline pH. The reversibility of PuO_2 NP aggregation is limited in concentrated electrolytes but is shown to be strongly facilitated by dilution with lower concentration electrolytes, carbonate-containing alkaline solutions, or simple addition of water, leading to efficient re-suspension of PuO_2 NP in solution at high pH. The data collected in this part of the project is the foundation for advanced thermodynamic modeling efforts discussed in more detail in Report Section 4.2.

4.2 Modeling of PuO_2 NP Reactivity in Concentrated Electrolytes

The following section is part of an article published in the Conference Proceedings of Waste Management Symposia 2025:

J. Neumann, B.A. Powell, D.A. Montgomery, R.E. Wilson, (2025). Colloidal behavior of plutonium oxide in concentrated electrolyte solutions. Waste Management Symposia 2025: Conference Proceedings, Article ID: 25207. https://www.osti.gov/biblio/2565226

Background. The available experimental data on PuO_2 NP stability in concentrated electrolytes is scarce, especially for electrolytes other than nitrate and particularly within the extreme electrolyte concentrations of the high-level waste tanks. The new collected data as part of this project (Section 4.1) provides a comprehensive set of stability ranges of PuO_2 NPs in highly concentrated electrolyte solutions of different anion composition (NO_3^-, Cl^-, ClO_4^-, SO_4^{2-}, $C_2O_4^{2-}$, CO_3^{2-}) at concentrations of up to 5 M, in both acidic and alkaline pH regimes. In Year 1, we tested state-of-the-art speciation models coupled to thermodynamic databases against the new experimental data by comparing it to the simulated dissolved [Pu], revealing important gaps and opportunities for improvement in respect to modeling approaches.

Methods. For estimation of speciation of Pu under the experimental conditions, the United States Geologic Survey program PHREEQC [14] was used along with the Nuclear Energy Authority (NEA) Thermodynamic Database [12]. Models predicting the impact of salt concentrations on [Pu] at acidic pH were run with a fixed pH of 1.5 whereas the experimental pH values shifted due to the presence of salts. For the prediction of [Pu] in the carbonate samples, the pH was fixed in the model to the experimentally measured value. It is noteworthy that many of the ionic strengths simulated in this work are outside the range of predictable values for the activity model within PHREEQC or there are no values for the specific ion interactions of the needed Pu-ligand species within the database. Therefore, the models should be evaluated as an approximation of the potential dissolved [Pu]. Furthermore, many of the measured [Pu] in this work represent both dissolved and colloidal Pu. However, the thermodynamic model does not contain any constants for prediction of colloidal species. Thus, the model predicts total dissolved Pu concentrations whereas the measured values are both aqueous and colloidal.

Modeling pH-dependent Pu Solubility and Colloidal Stability. The stability of the PuO_2 NP suspensions was studied over a broad pH range (1.5–12) by adding appropriate amounts of NaOH solution and measuring the resulting [Pu] (Section 4.1). The particle suspensions in the diluted electrolyte (0.05 M $NaNO_3$) are stable only under acidic conditions (pH < 3), whereas between pH 3–5, a decrease in [Pu] by two orders of magnitude is observed (Figure 19), indicating aggregation and subsequent sedimentation of the PuO_2 NPs.

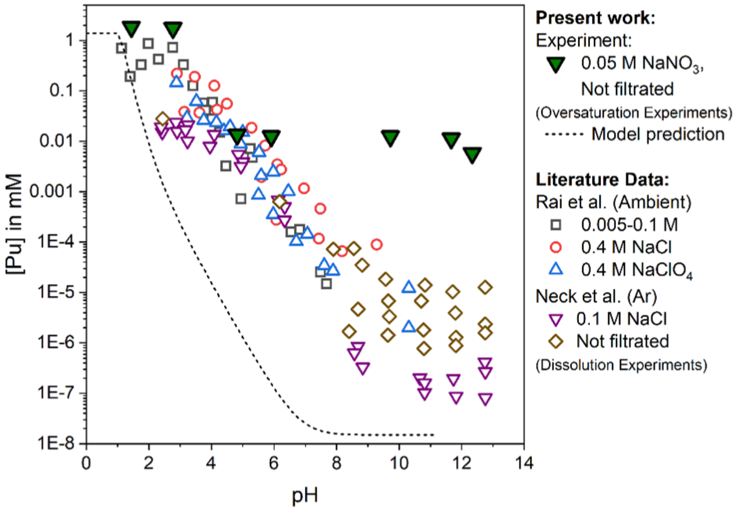

Figure 19. Predicted [Pu] based on thermodynamic modeling using PHREEQC at pe+pH = 10 (dashed line) compared to measured [Pu] in solution (filled symbols, section 4.1). Data are moreover compared to the experimental solubility of $PuO_{2+x(am,hyd)}$ as reported by Neck et al. (empty symbols, see [13] and references therein).

The decrease in [Pu] between pH 3–5 in our data is in agreement with data previously reported for the solubility of $PuO_{2+x(am,hyd)}$, that was measured by dissolution experiments of a Pu(IV) hydrous oxide precipitate (Figure 16). The two different approaches to measure solubility, i.e., from oversaturation (present work) vs. solid phase dissolution (Neck et al.), show significant deviations in [Pu] in the alkaline pH values. The lowest [Pu] are observed in samples prepared under Ar atmosphere after ultracentrifugation using 10 kD filters ($\sim 10^{-7}$ mM at pH >10), whereas [Pu] in samples that were not filtered were up to two orders of magnitude greater ($\sim 10^{-6}$–10^{-4} mM at pH >10). Moreover, samples prepared under ambient conditions showed elevated [Pu] in comparison to the samples reacted in Ar atmosphere at pH ~ 8 ($\sim 10^{-5}$–10^{-4} mM), indicating a potential impact of carbonate. All previously reported [Pu] determined through dissolution of Pu(IV) hydrous oxide precipitates are by at least three orders of magnitude lower than the [Pu] found for our samples ($\sim 10^{-2}$ mM at pH > 5) that contained pre-formed PuO_2 NPs and underwent an increase in pH by addition of NaOH. At these high pH values, attempts to thermodynamically model and simulate the dissolved Pu fraction underpredict our experimentally determined [Pu] by almost six orders of magnitude (dashed line in Figure 19), supporting the heavy influence of colloidal Pu in the alkaline pH regime.

Modeling Colloidal Stability in Concentrated Electrolytes. The impact of electrolytes on the colloidal stability of PuO_2 NPs was studied for a variety of electrolyte anions (NO_3^-, ClO_4^-, SO_4^{2-}, $C_2O_4^{2-}$, CO_3^{2-}) at acidic pH values (Figure 20, left, see section 4.1 for more details). Thermodynamic modeling of the nitrate, chloride, and perchlorate systems at a fixed acidic pH value (Figure 20, right) showed an increase in dissolved Pu with increasing salt concentrations due to formation of Pu(IV)-anion complexes (redox transformations were suppressed in this model). The predicted Pu-sulfate complexes in the model resulted in complete dissolution of the PuO_2, which disagrees with the experimentally observed decreasing [Pu] in solution. This indicates the potential thermodynamic stability of the colloids (which was not included in the model) compared to the dissolved Pu-sulfate complexes. Overall, the modeling results demonstrate the inability of current available thermodynamic models to predict the impact of salt addition on the [Pu] in solution for solutions containing PuO_2 NPs.

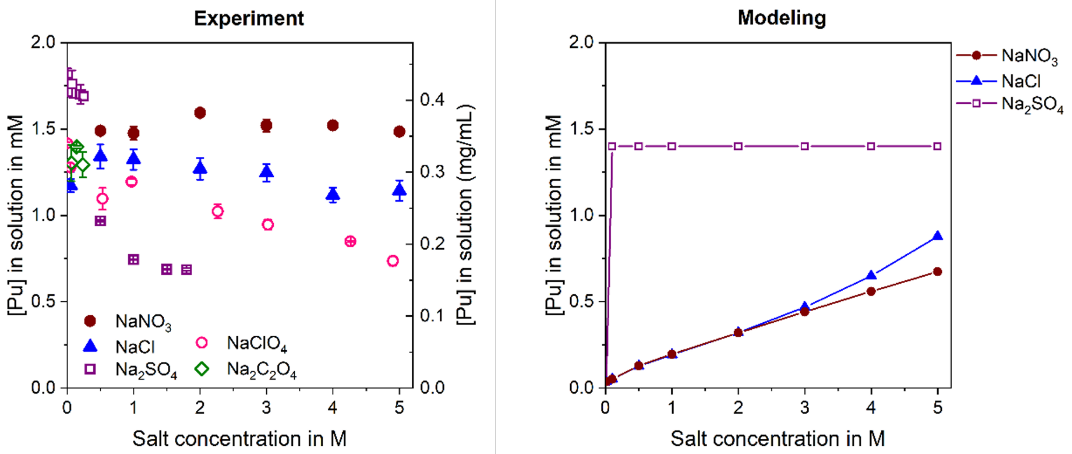

Figure 20. Changes in [Pu] in solution as function of salt concentration for different electrolytes as experimentally determined (left) and prediction of the effect of salt addition on the dissolved [Pu] by the currently available thermodynamic model (right), reflecting mostly the formation of metal-ligand complexes. Total [Pu] in the model was 1.4 mM and pH was fixed at 1.5 at constant pe+pH=10.

An additional modeling attempt was made for the chloride system, for which SIT parameters are available, allowing to account for changes in solution pH due to the salt addition. The model was successful in predicting the decrease in measured [Pu] with increasing pH (Figure 21, left), demonstrating the competition between chloride complexation and hydrolysis, i.e., at pH 1.5, the formation of the $Pu(OH)_4$ decreases the predicted [Pu] in solution drastically. However, it is noted that the precipitation of a solid $Pu(OH)_4$ as suggested by thermodynamic model is not observed experimentally, as the sample at the highest pH value of ~ 1.5 corresponds to the freshly synthesized and stable PuO_2 NP suspension.

Moreover, we tested the capability of the thermodynamic model to reflect the increased [Pu] in the carbonate-containing samples on the alkaline side (Figure 21, right). The model representing reducing conditions (pe+pH=10), i.e., Pu^{IV} is the dominant oxidation state and indeed, an increase in dissolved [Pu] is predicted by the model. However, the predicted speciation by the model leading to this elevated [Pu] is the Pu^{IV}-carbonate complex, indicating particle dissolution. Under more oxidizing conditions (pe+pH=20), the model predicts oxidation to Pu^{VI} and the dissolved Pu^{VI}-carbonate complex to be the dominant species, leading to a predicted [Pu] of 1.3 mM at carbonate concentrations greater than 0.25 M. In our experiments, the redox conditions were not controlled or measured; however, the solutions maintained a green color indicative of Pu colloids, consistent with characteristic PuO_2 NP spectroscopic signatures in Raman spectra. No experimental evidence of dissolved Pu^{IV} or Pu^{VI}-anion complexes were evident in the UV Visible absorption spectra of the carbonate samples. These results indicate that the thermodynamic stability of the PuO_2 NPs is greater than that of the Pu^{VI}-carbonate complexes.

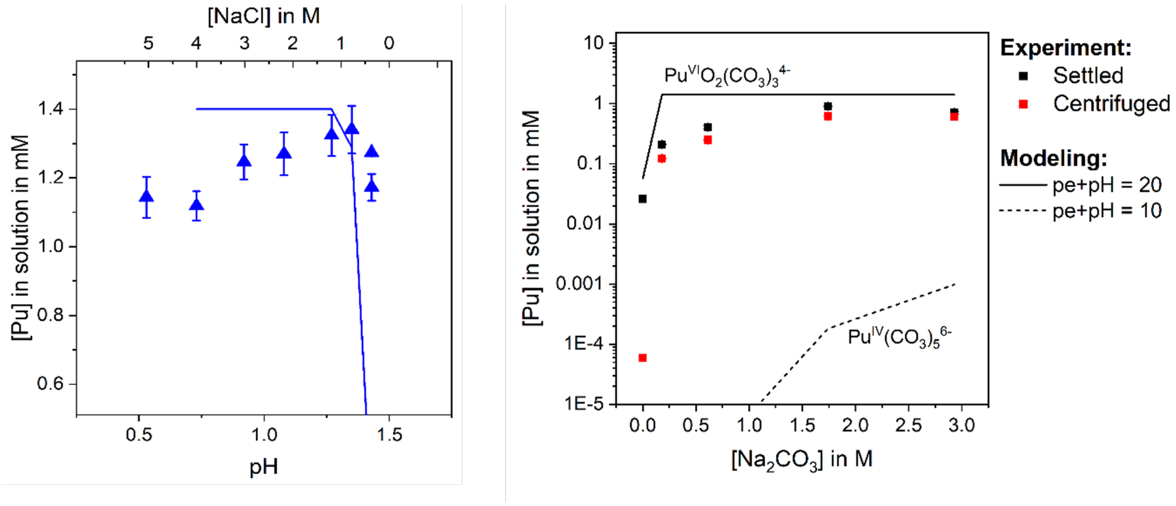

Figure 21. Comparison of [Pu] in solution (symbols) and model prediction (line) at total Pu concentration of 1.4 mM and variable pH (pe+pH=15) in the NaCl system (left). [Pu] in solution for Pu colloid reacted with Na_2CO_3 and comparison to the predicted [Pu] by the thermodynamic model (right), in which the pH values were constraint by the experimentally measured valued. The total Pu concentration in the model was 1.3 mM.

Conclusions and Outlook. Overall, the tested thermodynamic models were inadequate for predicting the experimentally observed [Pu]. The ionic strengths examined in this work are beyond the range for accurate predictions using the current thermodynamic models and data. However, the general trends can be compared. Formation of Pu-anion complexes clearly impacted the experimental data and was demonstrated in the models. However, the models do not contain any thermodynamic data for colloids and comparison between the experimental and modeling efforts demonstrate that the thermodynamic stability of Pu colloid phases is needed for a complete thermodynamic description of Pu behavior in these systems. Specifically, the Pu-sulfate and Pu-carbonate systems were predicted to be completely dissolved despite the clear observations of colloids in experimental work, indicating the thermodynamic favorability of Pu colloidal phases over the aqueous complexes. Further studies specifically focused on determining the thermodynamic parameters needed to describe Pu colloids under acidic and alkaline, as well as low and high ionic strength conditions are required for accurate predictions of Pu speciation. The comprehensive experimental dataset collected in this work (Sections 4.1 and 5), consisting of solubility data correlated to spectroscopically determined aqueous speciations quantitatively informing about changes in Pu oxidation states and amounts of dissolved Pu-anion complexes presents a promising opportunity to attempt the development of a more accurate thermodynamic description of solutions of PuO_2 NPs in diluted and concentrated electrolytes, which will be a focus of Years 2 and 3.

4.3 PuO_2 NP Aging Under Tank Waste Conditions

Brian A. Powell, Dawn A. Montgomery, Rhianna Wolsleger

Approach. A series of batch experiments was designed to characterize the behavior of PuO_2 NPs under tank waste conditions. These included experiments in sodium nitrate concentrations ranging from 0.01 to 4 M, initial pH values of 6, 11, and 14, in the presence or absence of crystalline silica titanate (CST, see section 6 for more details on material) or monosodium titanate (MST), and in the presence or absence of iron. The experimental set consisted of 39 Teflon reactor vessels which were held in an anoxic glovebox in a dry heat bath at 35 °C. The samples were spiked to 0.20 mM total ^{239}Pu as PuO_2 NPs and sampled after 90 days of equilibration. Note that for experiments with CST and MST added, the sorbent material was not added to the reactors until 33 days after the initiation of the experiment. All samples continue to age and the sampling procedure described below will be repeated with additional microscopic and spectroscopic characterization of the aqueous and solid phases. The experimental matrix and objectives for each variable are described in Table 3.

Table 3. Experimental matrix for PuO_2 NP aging experiments. All experiments in 7 mL Teflon vials with 0.2 mM ^{239}Pu as PuO_2 NPs.

Inital pH	$[NaNO_3]$ in M	CST/MST presence	Fe presence	Objective
6, 11, 14	0.01, 0.1, 1, 3, 4	No	No	Observe the influence of pH and $[NaNO_3]$ on PuO_2 NP stability
6, 11, 14	0.1, 4	No	Yes	Observe potential co-precipitation or sorption of PuO_2 NPs by Fe precipitates
11, 14	0.1, 1, 4	Yes	No	Examine partitioning of PuO_2 NPs to CST and MST
11, 14	0.1, 1, 4	Yes (only CST)	Yes	Examine impact of Fe precipitation on partitioning of PuO_2 NPs to CST

The intent of these experiments is to age the samples for at least 6 months prior to detailed microscopic and spectroscopic characterization using transmission electron microscopy (TEM), Raman spectroscopy, and X-ray photoelectron spectroscopy (XPS). Selected samples may be taken for X-ray absorption spectroscopy should preliminary data indicate it would be useful. The initial sampling event after approximately 3 months consisted of:

1. Removing an aliquot of the sample without mixing to evaluate the concentration of dissolved Pu plus colloidal PuO_2 (referred to as “settled” sampling in this report).
2. Filtration of the aqueous phase through a 3k polyesthersulfone (PES) ultrafiltration membrane.
3. Measurement of the pH and oxidation reduction potential (ORP) of the aqueous phase.

A systematic study of multiple ultrafiltration membranes materials and sizes was performed prior to sampling to determine that the 3k PES membranes were suitable for this work (data not shown). Aliquots of each solution were counted on a 2910 Tricarb Liquid Scintillation Counter (LSC) to determine the Pu concentration. For samples below the LSC detection limits, samples were run on a Thermo iCAP RQ ICP-MS which had approximately a 100x lower detection limit.

Results. Both pH and $NaNO_3$ concentration impacted the concentration of Pu remaining in the aqueous phase after 90 days of equilibration. In all cases, there was over a 99% reduction in the initial 0.2 mM concentration of Pu indicating a high amount of particle aggregation occurred at higher pH values, consistent with observations in the reactivity studies conducted in Section 4.1. The initial PuO_2 NP solution was stable in 10 mM HNO_3. The target pH values of the solutions were 6, 11, and 14 and the average pH values measured during sampling were 5.8, 10.8, and 13.4. Introduction of the PuO_2 NPs to a neutral or high pH facilitates aggregation and settling of the colloids. Ongoing experiments examining PuO_2 NP surface chemistry seek to examine the surface charging effects leading to such aggregation (Report Sections 5 and 2.2). It is notable that a higher concentration of PuO_2 NPs remains in solution at pH 14 compared with pH 11. Thus, it is possible that a higher negative particle surface charge induced in pH 14 solutions may yield greater PuO_2 colloid stability. Furthermore, there is an increase in Pu concentrations with increasing $NaNO_3$ for the solutions with only settling compared to those from filtration. Thus, it does not appear that an aqueous $Pu(NO_3)_x^{4-x}$ complex is the major source of the increase in Pu concentrations at higher $NaNO_3$ in the “settled” samples from Figure 22A, despite the fact that absorption spectroscopic investigations showed some particle dissolution at elevated nitrate concentrations, indicating a small contribution of $Pu(NO_3)_x^{4-x}$ to the Pu speciation (<20 %, see section 5.1).

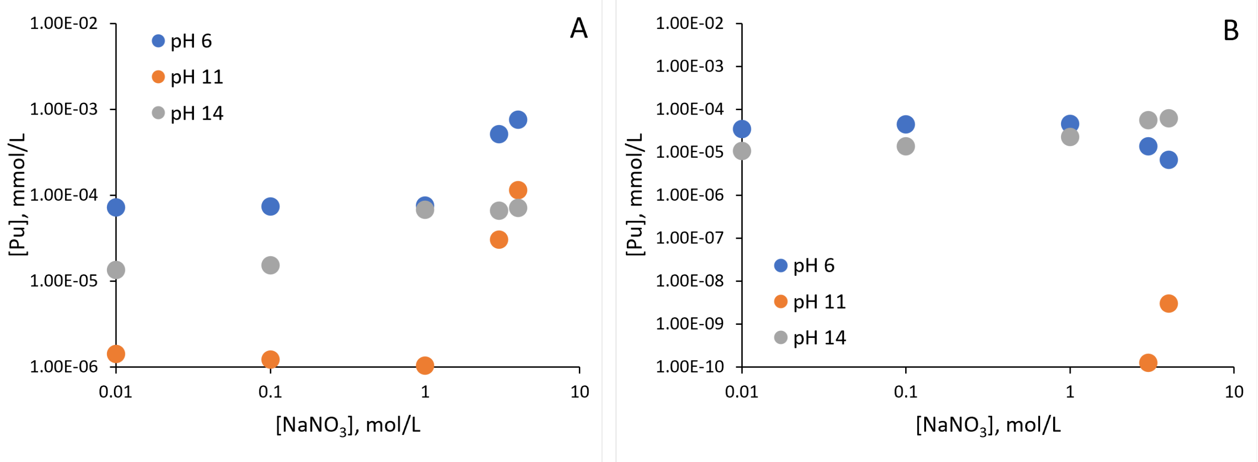

Figure 22. Concentrations of Pu remaining in aqueous phase after settling (A) and after filtration (B) as a function of pH and $NaNO_3$ concentration. Sampling occurred after 90 days of equilibration at 35 °C. Note, Pu concentrations in filtered solutions at pH 11 are near ICP-MS detection limits.

Impacts of CST and MST addition. Addition of CST to the reaction vessels occurred after samples had been reacting for 33 days in order to examine the impact of CST addition on PuO_2 NPs that remain in solution after the initial aggregation occurred. The addition of CST caused further reductions in the aqueous concentration of Pu at pH $\sim$9 and $\sim$13.5. The initial pH of solutions were targeted at 11 and 14 but after equilibration averaged 9 and 13.5 indicating there was some pH buffering of the CST at lower pH values (Figure 23). Furthermore, there was a decrease in concentration between the settled and filtered samples, indicating that the CST did not fully remove colloidal PuO_2 remaining in suspension. Comparison of the measurements of Pu concentrations after settling in samples with and without CST indicates that PuO_2 NPs appear to have relatively little affinity for CST at lower ionic strengths. Note that the samples with initial pH values of 11 are not directly comparable as the average pH for the CST bearing samples was 9 and average for samples without CST was 10.8. At both pH values, there appeared to be removal of PuO_2 NPs in 4 M $NaNO_3$ conditions by CST. Thus, the interaction between PuO_2 NPs and CST could potentially be facilitated by nitrate interactions with CST and the PuO_2 NP surface. Additional experiments using MST were performed and comparable results were observed (not shown).

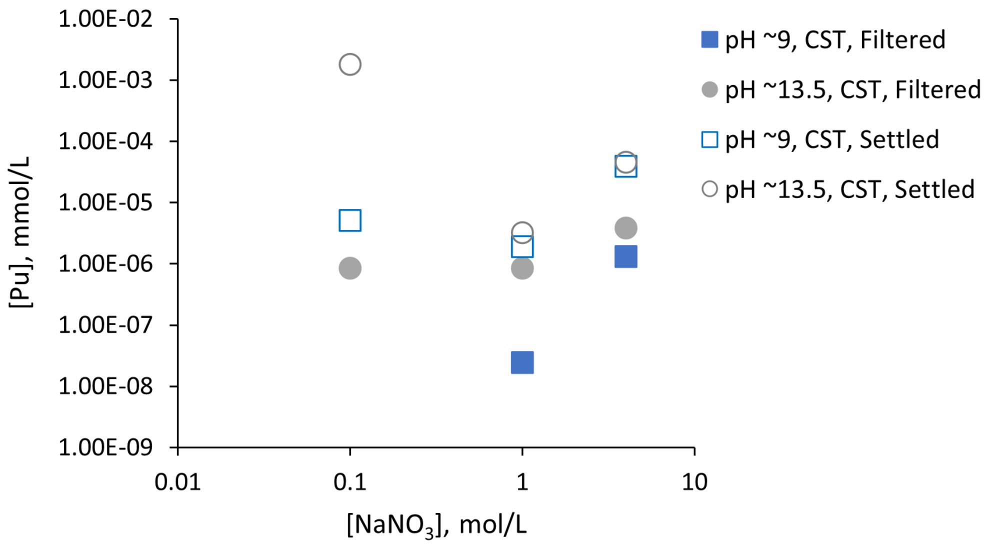

Figure 23. Measured Pu concentrations after settling (open symbols) and filtration (closed symbols) in reactors containing CST.

Table 4. Measured Pu concentrations after settling in samples with and without CST.

Initial pH	[$NaNO_3$] in M	[Pu, CST] in mM	[Pu, no CST] in mM	[Pu, CST]/[Pu, no CST][a]
11	0.1	$5.1\cdot10^{-6}$	$1.2\cdot10^{-6}$	4.2
11	1	$1.9\cdot10^{-6}$	$1.0\cdot10^{-6}$	1.8
11	4	$3.9\cdot10^{-5}$	$1.2\cdot10^{-4}$	0.34
14	0.1	$1.8\cdot10^{-3}$	$1.5\cdot10^{-5}$	120
14	1	$3.2\cdot10^{-6}$	$6.8\cdot10^{-5}$	0.05
14	4	$4.5\cdot10^{-5}$	$7.1\cdot10^{-5}$	0.63

[a] Settled measurements.

Impacts of Fe addition. Several tanks also contain high levels of iron used during chemical processing. Thus, the project sought to examine potential impacts of iron on PuO_2 NP stability. The addition of iron to samples initially at pH 6, 11, and 14 and $NaNO_3$ concentrations from 0.1 to 4 M resulted in rapid precipitation and a reduction in pH due to iron hydrolysis. Separate samples without Pu present were also prepared and it was shown that the iron oxyhydroxide mineral goethite was the dominant phase. The decreased pH had a major impact on the concentrations of Pu in solution wherein lower pH values yielded much higher concentrations of Pu, comparable to the observed stability of PuO_2 NPs in the low pH working solution used to spike these experiments (Figure 24A). It is noteworthy that the Fe was added after the PuO_2 NPs were spiked into the solutions. Thus, aggregation of the PuO_2 NPs likely occurred and the lowering of the pH due to addition of Fe appeared to have caused re-suspension/de-aggregation of the colloids. The impact of pH is also shown in samples where both Fe and CST were added due to the CST buffering the pH near 5 and preventing the low pH conditions (Figure 24B). There is a systematic decrease in Pu concentrations with increasing pH in these data. It is noteworthy, that in the presence of Fe, Pu was nearly quantitatively removed from solution in higher pH solutions both in the presence and absence of CST.

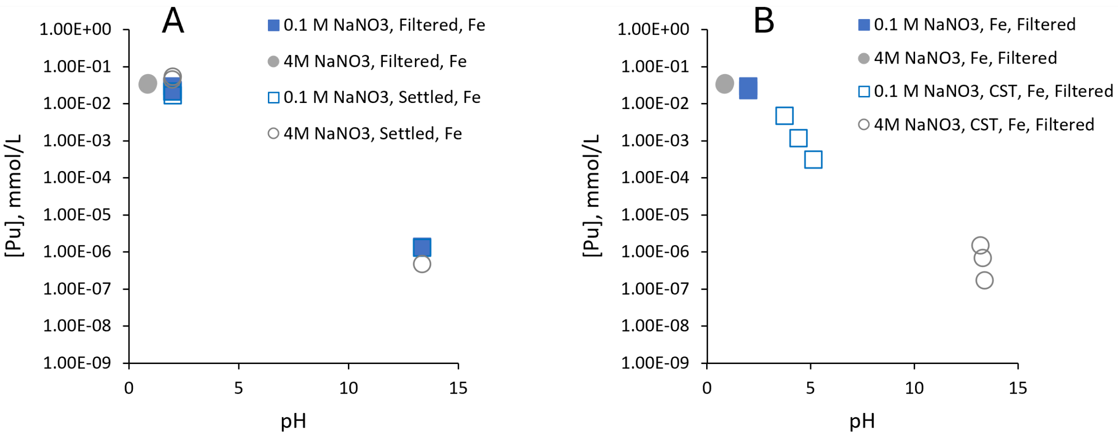

Figure 24. (A) Measured Pu concentrations after settling (open symbols) and filtration (closed symbols) in samples with Fe added. (B) Measured Pu concentrations after settling (open symbols) and filtration closed symbols) in samples with Fe added and CST added.

Conclusions and Outlook. A systematic series of batch experiments was conducted to investigate the behavior of PuO_2 NPs under simulated Hanford tank waste conditions. All samples continue to age and the sampling procedure described above will be repeated with additional microscopic and spectroscopic characterization of the aqueous and solid phases. The findings advance our understanding of PuO_2 NP colloidal stability and reactivity under conditions relevant to Hanford tank waste environments. The results highlight the influence of pH, ionic strength, and sorbent materials on Pu speciation, aggregation, and partitioning on sorbent materials. The observed interactions between PuO_2 NPs and CST/MST, as well as the role of iron precipitation, underscore the complexity of Pu chemistry in high-salinity, high-pH environments. Understanding the reactivity under these conditions on a molecular scale is essential for improving thermodynamic models and enabling reliable predictions of PuO_2 NP chemical speciation under diverse solution conditions. Such predictive capabilities are crucial for informing long-term waste management strategies and ensuring the safe handling of nuclear waste at sites like Hanford.

5 Characterization of PuO_2 NPs Surface Chemistry using Spectroscopic Methods

5.1 Insights into Reactivity of PuO_2 NPs in Concentrated Electrolytes by Optical Absorption Spectroscopy

Julia Neumann, Richard E. Wilson

Background. Optical absorption spectroscopy provides a powerful, non-invasive technique to probe the electronic transitions and structural dynamics of chemical species under varying chemical conditions. Tetravalent Pu has the ground state electronic configuration of $5f^4$ and its absorption spectrum is dominated by f-f transitions that are parity forbidden in the highly symmetric Pu^{4+} aquo ion. As the crystal structure of PuO_2 is highly symmetric (fcc structure), the absorption bands in its absorption spectrum are caused mainly by vibronic transitions [15]. The absorption spectrum of PuO_2 NPs was reported to be similar to crystalline PuO_2, indicating similar structural properties of the two materials, including vibrational modes and their energies [15].

Since its first report, the characteristic spectrum of PuO_2 NPs with its absorption bands at 510, 578, 615-630, 688, and 735, 817 nm [16, 17] has been used by many groups to identify the presence of Pu colloids in aqueous and organic solutions [2, 15–20]. Minor spectral changes were reported based on sample preparation (hydrolytic vs. sonoloytic) [17], colloid aging [20], and solution conditions like pH [19]. While the measured absorptivity ($\varepsilon_{615} \sim 13$ $M^{-1}cm^{-1}$ [17]) can be used to estimate PuO_2 NP concentrations in solution, the uncertainty of such measurements were reported to be high due to broad particle size distributions. Only one example reports significant changes in the optical spectrum for plutonium(IV)-silicate colloids, with absorption bands at 455, 486, 526, 551, 584, 633, 654, 677, 755, 793 nm [21], indicating that absorption spectroscopy can be used as structural characterization tool for PuO_2 NPs. Therefore, this part of the current project aims to explore systematically the use of absorption spectroscopy to study the surface reactivity of PuO_2 NPs, with the goal to gain a predictive understanding and control of the chemistry of these capricious species in the Hanford waste treatment processes.

Methods. Sample preparation followed the procedure decribed in more detail in sections 3 and 4.1 of this report. High-resolution absorption spectra were collected using a Cary 6000i UV-Vis-NIR spectrometer and 1 cm plastic cuvettes. Spectra were collected (350-1100 nm, exposure time = 0.1s, step width = 0.25 nm, spectral bandwidth: 0.75 nm) and measured against a water blank. Additional datasets of control measurements showing the evolution of the electrolyte background with increasing salt concentrations are available but are not shown here.

Synthesis of PuO_2 NPs in Mineral Acids and Aging. Report Section 3 discusses the synthesis of PuO_2 NPs in different mineral acids, with the main findings that differences in particle properties are found mostly in the first few days of the reaction, after which the particle properties in the different media are the same. The particles were characterized by absorption spectroscopy during the synthesis to track structural changes in the beginning of the synthesis and throughout the aging process (Figure 25).

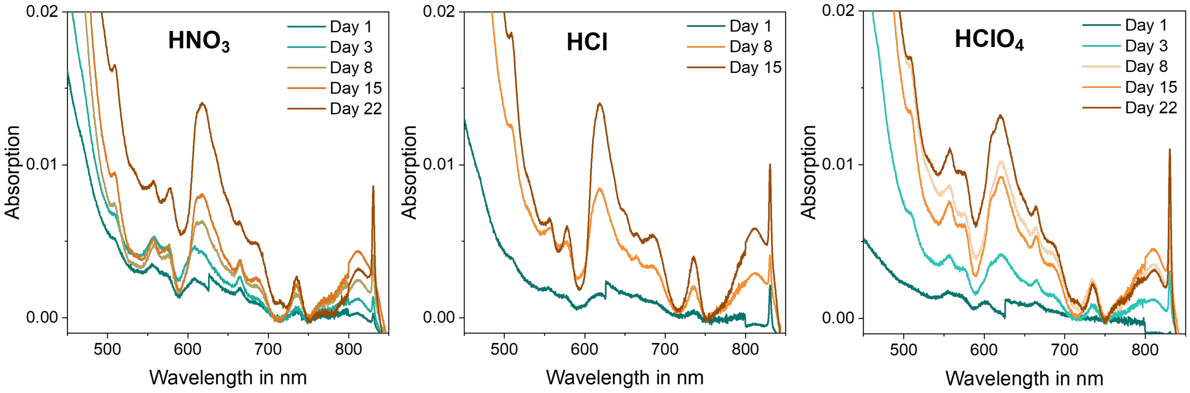

Figure 25. UV Visible Absorption spectra of PuO_2 NPs synthesized from different mineral acids over time. Day 1 spectra show an additional feature at 626 nm caused by switching of the light source in the instrument during the measurement.

All spectra show the characteristic absorption bands for PuO_2 NPs at 509, 577, 610, 618, 687, and 736 nm that are consistent with the reported values for Pu colloids [16, 17]. Minor differences are identified in relative peak intensities between 620-700 nm. These observations are consistent with the results discussed in section 3 that particle properties in the various mineral acids are overall very similar after the initial phase of the synthesis.

Three additional bands are found in the spectra in Figure 25 at 557, 666, and 831 nm. The narrow and intense band at 831 nm can be assigned to Pu^{VI} [22], formed by disproportionation of Pu^{IV}. Based on the molar absorptivity of this band (555 $M^{-1}cm^{-1}$ [23, 24]), the contribution of Pu^{VI} to the overall speciation is determined to be <1% at any given time during the syntheses. The other two additional absorption bands at 557 and 666 nm are notably close to bands of Pu^{3+} [22], although it is striking that the third band that would be expected for Pu^{III} at 600 nm (that has a similar molar absorptivity as the band at 557 nm) is absent in our spectra, making the assignment of these bands to Pu^{III} questionable. If the bands were indeed to correspond to Pu^{III}, then its contribution to the speciation based on the band intensity at 557 with a molar absorptivity of 33.8 $M^{-1}cm^{-1}$ [22] would be significant, ∼8-10% on Day 8 of the synthesis. It is noted that, in the nitrate case, the formation of Pu^{III} nitrate complexes would lead to a shift of the band at 557 to 564 nm but not of the band at 600 nm [25], both of which are not observed in our experimental data, another indication that the two bands at 557 and 666 nm are likely not caused by Pu^{III}.

In the first few days of the synthesis, the symmetry of the most intense absorption band at ∼610-620 nm changes slightly from a higher intensity at 610 nm at earlier stages of the synthesis towards 620 nm over time (Figure 25). A shift of the absorption band from 630 to 620 nm upon colloid aging, as described by Walter et al. [20], is not seen here. This may be caused by the different synthesis approaches, i.e., hydrolysis of $Pu(OH)_4$ precipitate in dilute mineral acid here vs. slow titration of a Pu^{4+} solution by dilute acid or NaOH in Walter et al., in which the feature at 630 nm was observed at pH 0.4-1.4, indicating that it possibly corresponds to small oligomeric precursors during the initial stages of particle formation. We will continue to track the spectral evolution over time to identify potential additional changes upon further aging of the PuO_2 NPs.

While no significant shifts in the absorption spectra are observed, an overall increase in intensity of the absorption bands, consistent with the increasing concentration of PuO_2 NPs over time (Figure 12), becomes evident. As the contribution of other Pu oxidation states to the measured [Pu] through LSC are <1 %, we can estimate the molar absorptivities of PuO_2 NPs from our series of spectra measured in HNO_3, HCl, and $HClO_4$. The Lambert-Beer plots are shown for two absorption bands, 618 and 735 nm, in Figure 26. Linear fits yield molar extinction coefficients of 9.2±0.9 $M^{-1}cm^{-1}$ for ∼618 nm and 2.0±0.3 $M^{-1}cm^{-1}$ at 735 nm, valid for diluted solutions of ∼0.05 M background electrolyte. It is noted that the latter value seems more reliable given that it slightly less impacted by the complicated spectral background of the PuO_2 NPs due to Mie scattering. The value determined for 618 nm is slightly lower than the value estimated recently by Micheau et al. based on a very limited spectral dataset (ε_{615} ∼13 $M^{-1}cm^{-1}$) [17].

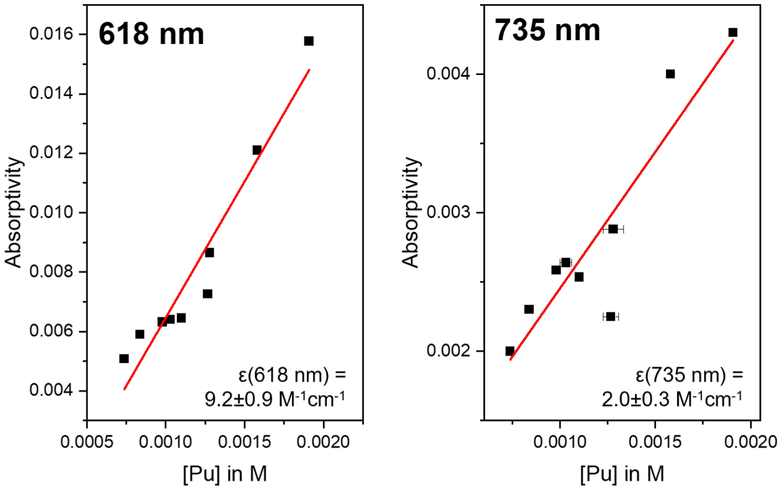

Figure 26. Background corrected absorptivity of two absorption bands of PuO_2 NP spectra shown in Figure 25 and their correlation to [Pu] determined by LSC as shown in Figure 12. The data were used to determine the molar extinction coefficients ε for the two absorption bands according Beer's Law (Abs = $\varepsilon \cdot c \cdot d$), with Abs = Absorptivity, c: concentration, d: sample path length.

Spectral Evolution from Diluted to Concentrated Solution. Next, as part of the characterization of the reactivity of PuO_2 NPs in concentrated electrolytes (Section 4.1), we studied whether spectral changes indicated changes in the surface structure of the particles. Absorption spectra were collected for series of concentrations of $NaNO_3$, NaCl, and $NaClO_4$ (Figure 27, right). While the spectra in $NaClO_4$ are mostly unaffected by the high salt concentration, major changes are observed in NaCl and $NaNO_3$, indicating interactions of the electrolyte anion with the particle surface. In chloride, peaks at 653 and 666 nm increase in intensity and a broad absorption band from 628-714 nm increases the intensity in respect to the characteristic PuO_2 NP at 618 nm that is shifted in its peak maximum from ~620 to 613 nm in 5 M NaCl. Additionally, the peak ratio of the bands at 558 and 578 nm reverses, with the latter being the more intense peak in diluted solution, while the former is the dominant peak in the concentrated NaCl solution. Similar spectral changes are observed in the $NaNO_3$ samples. Absorption from 625-687 nm increases significantly, causing the two most intense absorption bands to be at 638 and 661 nm, which is significantly different from the PuO_2 NP spectrum in diluted solution. A minor shift and change in the shape of the peak at ~ 620 nm to 623 nm is found in $NaNO_3$ that is reversed to the trend observed in NaCl, indicating differences in the interaction mechanisms of the two ligands with the particle surface.

The current work demonstrates the first observation that absorption spectroscopy can be a suitable probe for the surface structure of PuO_2 NPs and can therefore be useful beyond the mere identification of colloidal species in Pu samples. Many open questions remain regarding the exact interpretation of the observed spectral evolution upon changes in the particle surface structure. Additional work that includes the combination of other surface-sensitive spectroscopic and scattering techniques will be required to gain deeper insights into the origins of the observed spectral changes.

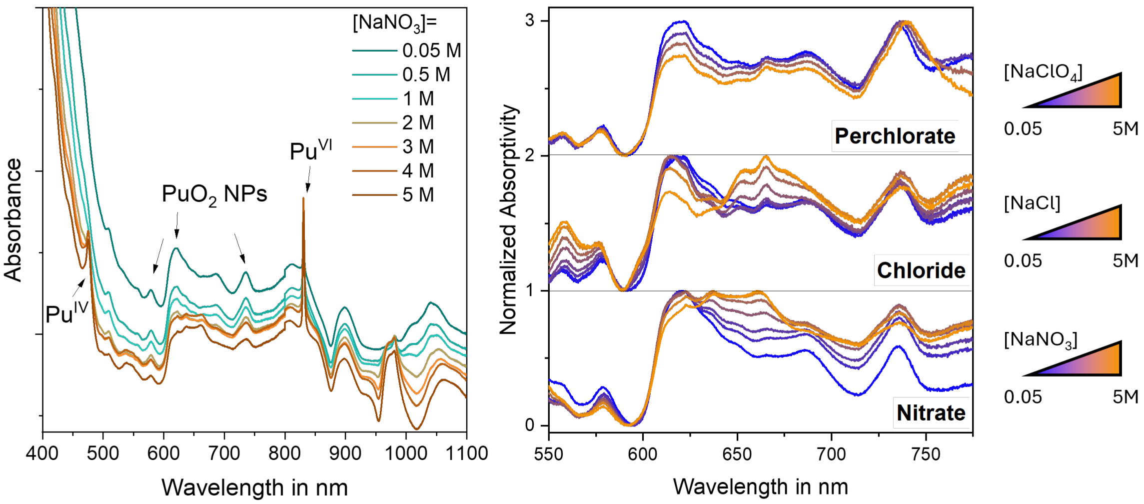

Figure 27. UV Visible Absorption spectra of PuO_2 NPs reacted with inorganic electrolytes. Left: Full set of spectra examplarily shown for $NaNO_3$, Right: Background corrected and normalized spectra truncated to the characteristic spectral region of PuO_2 NPs to emphasize the spectral evolution with increasing salt concentration.

Dissolution of PuO_2 NPs in Concentrated Electrolytes. While the use of absorption spectroscopy to elucidate surface reactivity of PuO_2 NPs is still under development, it is an established tool to quantify the Pu speciation, specifically the contributions of different Pu oxidation states that are formed through disproportionation of Pu^{IV}, according to:

$$2\,Pu^{4+} + 2\,H_2O \leftrightharpoons Pu^{3+} + PuO_2^{+} + 4\,H^{+}$$
$$3\,Pu^{4+} + 2\,H_2O \leftrightharpoons 2\,Pu^{3+} + PuO_2^{2+} + 4\,H^{+}$$

Absorption spectra were collected for PuO_2 NPs reacted with increasing concentrations of $NaNO_3$, NaCl, and $NaClO_4$. Upon salt addition, the spectra in NaCl and $NaNO_3$ show additional peaks at 470 and 476 nm, respectively, whose intensity increases with increasing salt content. These peaks can be assigned to Pu^{4+} and $Pu(NO_3)^{3+}$/$Pu(NO_3)_2^{2+}$ [22, 26, 27], respectively. Similarly, changes in the sharp absorption band at 831 nm are identified. In all three electrolytes, the band intensity increases strongly with increasing salt level, and in NaCl, an additional band at higher wavelength (838 nm) appears, indicating the formation of $PuCl^{3+}$ [24].

Based on the molar extinction coefficients of Pu^{IV} (49 $M^{-1}cm^{-1}$, [22]) and Pu^{VI} (555 $M^{-1}cm^{-1}$, [23, 24]) and under the simplification that extinction coefficients do not vary as function of ionic strength, we can determine the contribution of dissolved Pu^{IV} and Pu^{VI} to the Pu speciation in the concentrated electrolytes (Figure 28). The concentrations of Pu^{IV} and Pu^{VI} are subtracted from the measured total [Pu] via LSC (cf. Figure 14, left) that includes PuO_2 NPs, Pu^{IV}, and Pu^{VI} to yield the concentration of PuO_2 NPs in solution. Significant differences in the species distribution in the three investigated electrolytes are identified. First, the amount of Pu^{IV} formed in the samples containing concentrated NaCl and $NaClO_4$ is very small (<1 %). In contrast, in 5 M $NaNO_3$ ∼26% of the Pu in solution is present as dissolved mononuclear Pu^{IV} species, mostly $Pu(NO_3)^{3+}$ and $Pu(NO_3)_2^{2+}$ that cannot be distinguished from each other based on their absorption spectra alone [26, 27]. While the amount of Pu^{IV} in chloride media is negligible, significant amounts of Pu^{VI} are identified, ∼12% in 5 M NaCl. This is considerably more than in nitrate (4%) and perchlorate (7%).

Overall, absorption spectroscopy reveals that PuO_2 NPs are most stable against dissolution in perchlorate media. Particle dissolution is considerably stronger in chloride media, resulting mostly in Pu^{VI} in solution, and strongest in nitrate under the formation of Pu^{IV}, indicating substantial differences in the reactivity of the two systems. In perchlorate, salt addition leads mainly to particle aggregation and sedimentation, which is reflected in the decrease in [Pu] measured by LSC. In contrast, in chloride and nitrate, the measured [Pu] in solution remains almost unchanged even at 5 M salt. The PuO_2 NP concentration in these solutions decreases just like in the perchlorate case, just not through aggregation and sedimentation but through dissolution, followed by two very distinct solution pathways resulting in Pu^{IV} being the dominant dissolved mononuclear species in concentrated nitrate and Pu^{VI} in chloride media. These two solution pathways are most likely controlled by the combination of chloro/nitrato complexation of Pu^{IV} and Pu^{VI}, as well as subtle differences in redox potentials in chloride and nitrate media that affect the disproportionation of Pu^{IV}. Importantly, the quantitative species distribution determined from absorption spectra in combination with the solubility data measured by LSC provides a robust data foundation for advanced thermodynamic modeling of PuO_2 NP solutions that is the focus of Report Section 4.2

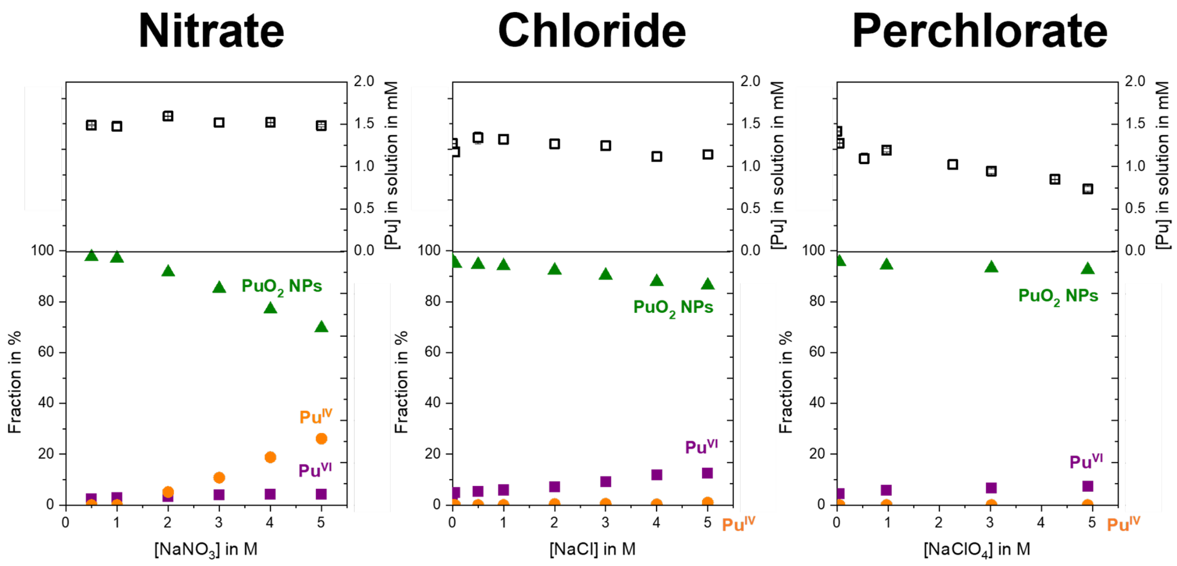

Figure 28. Correlation of [Pu] measured by LSC (black symbols, cf. Figure 14) with the speciation of the soluble Pu fraction as observed from absorption spectroscopy (cf. Figure 27) for the three studied electrolytes.

5.2 Surface Interactions of Inorganic and Organic Ligands with PuO_2 NPs

Julia Neumann, Richard E. Wilson

Background. In addition to the electrolyte anions discussed in the previous section, we tested a series of organic and inorganic complexing ligands towards their affinity to bind to the PuO_2 NP surface. Besides absorption spectroscopy, we also applied Raman spectroscopy as additional powerful structural probe. Many of the investigated ligands have characteristic Raman signatures that can give insights into binding to the particle surface. Moreover, based on group theoretical analysis, the crystalline PuO_2 core of the particles with their cubic fcc structure have only one Raman-allowed transition, the T_{2g} mode that is typically observed in bulk PuO_2 at 476-479 cm^{-1} [28]. In nano-confinement, this T_{2g} band shifts strongly to lower energy (red-shift), and its band position and width can serve as measure for the crystallite size [29–32]. Additionally, it has been established that defects in the crystal structure and as well as surface effects cause a decrease in crystal structure symmetry that allows the appearance of additional bands, often referred to as 'defect bands', around 580 and 650 nm [33]. Therefore, the intensity of these defect bands give insights into the crystalline character of the PuO_2 NP core.

Initial tests were conducted in the acidic pH regime, as a higher PuO_2 NP concentration in solution simplifies UV Visible absorption spectroscopic characterization. Within the scope of the project, we selected three Hanford-relevant ligands: sulfate, acetate, and oxalate for the initial work and complemented these datasets with trichloro acetic acid (TCA) and glycine as two ligands that are known to associate strongly with polynuclear Pu species [2, 34]. The ligands display a series of increasing Broensted acidity, i.e., the ability to donate a H^+, that controls their ability to form complexes in solution and bind to surfaces of solids (including particle surfaces). The deprotonation of the ligands is generally described by: $HA + H_2O \leftrightarrows A^- + H_3O^+$, with the corresponding deprotonation constants pK_a of the studied ligands compiled in Table 5.

Table 5. Compilation of deprotonation constants (pK_a) of studied ligands.

Ligand	Sulfate	TCA	Oxalate	Glycine	Acetate
pK_a	-3, 1.99	0.60	1.27, 4.38	2.34	4.76
Experiments:					
[Ligand] in M	0.01-1.8	0.015	0.002	0.01	0.01
Observation	Aggregation/Sedimentation		Aggregation/Dissolution[a]	Stable Colloidal Suspension	

[a] Dissolution of PuO_2 NPs synthesized in HNO_3, Aggregation and precipitation of PuO_2 NPs synthesized in HCl and $HClO_4$.

Methods. Samples at acidic pH were prepared according to the procedure described in section 4.1. The pH was not controlled but monitored and shifted to slightly higher values upon salt addition (pH=1.7-2.4). Raman samples at alkaline pH were prepared by using an acidic PuO_2 NP solution that was neutralized to pH 13.8 by addition of NaOH, leading to aggregation of particles. Solutions of diluted or concentrated $NaNO_3$, NaCl, $NaClO_4$, as well as oxalate, sulfate (Na_2SO_4), and carbonate (Na_2SO_4) were added to aliquots of this PuO_2 NP coagulate and reacted for three weeks. After that, a small amount of the samples was dried on a glass slide and characterized for (i) impact of the electrolyte on the particle crystallinity, and (ii) particle surface-ligand interactions using Raman spectroscopy.

Ligand-Association at Acidic pH. Preliminary experiments showed that the addition of acetate and glycine to PuO_2 NP solutions at acidic pH did not lead to any visible particle aggregation or spectral changes. It is likely that the experimental pH values in these initial tests were too acidic, so that the ligands were protonated in solution and therefore not available to bind to the PuO_2 NP surface. Additional tests at higher up to alkaline pH will be carried out to study the ligands' impact on preventing pH-induced PuO_2 NP aggregation and sedimentation.

In contrast, the addition of sulfate and TCA leads to visible particle aggregation and sedimentation. For sulfate, this leads to a decrease in [Pu] in solution from 1.77 mM in the absence of sulfate to at 1.69 mM at 0.25 M Na_2SO_4 to 0.69 mM Pu at 1.8 M sulfate (Figure 29, top right). Absorption spectroscopy showed significant spectral changes, even at low sulfate concentrations 29, indicating changes in the Pu speciation. First, a narrow and intense absorption band at 480 nm is identified and can likely be attributed to $PuSO_4^{2+}$, which is expected to have a significantly shifted band position compared to Pu^{4+} (470 nm [22]). No Pu^{VI} is found at any sulfate concentration. Moreover, the sulfate-adsorbed PuO_2 NPs have low intensity absorption bands at 511, 546, 564, 616, 653, 674 and 734 nm, which is significantly shifted compared to the as-synthesized PuO_2 NPs. The reversal in the zeta potential of the PuO_2 NPs, as discussed in detail in Report Section 4.1, suggest strong interactions of sulfate with the PuO_2 NP surface. These strong interactions are further confirmed by the significant changes in the absorption spectra that clearly demonstrate

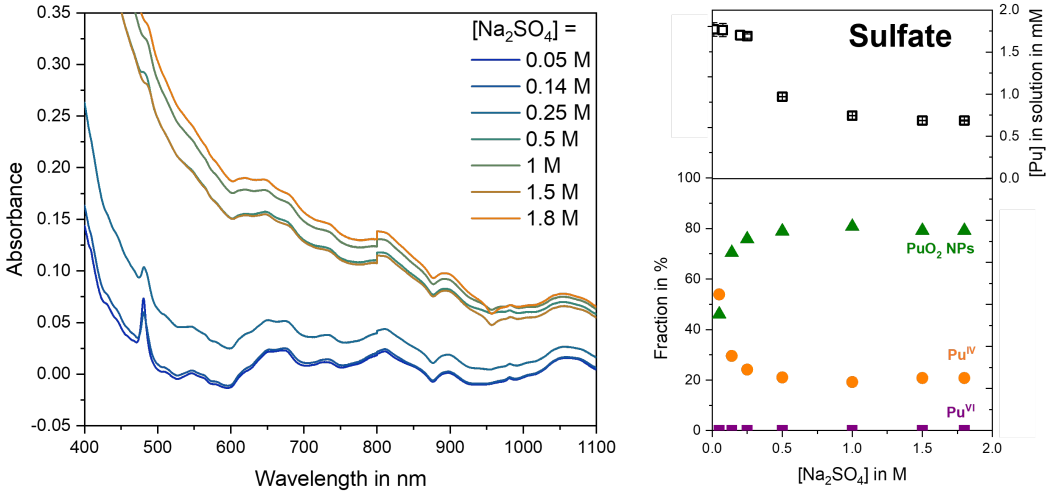

Figure 29. Left: UV Visible absorption spectra of PuO$_2$ NPs reacted with varying concentrations of Na$_2$SO$_4$. Right: UV-visible absorption spectroscopy was employed to extract contributions of PuO$_2$ NPs and dissolved Pu(IV) and Pu(VI) species to the speciation, which was then correlated to the measured solubility data.

surface-sensitivity towards ligand-association. Comparing the absorption spectra of the sulfate-adsorbed PuO$_2$ NPs to that of plutonium(IV)-silicate colloids [21] reveals limited overlap in the positions of individual absorption bands, suggesting either fundamental differences in the core structure of the two types of colloids or spectral sensitivity towards which ligand is bound on the particle surface. However, notable similarities in the overall spectral features are evident, including a broad absorption band between 600-700 nm and a distinct double band feature at ∼750 and 800 nm.

Based on the absorption spectra, the Pu speciation in the sulfate system was analyzed. As can be seen in Figure 29, bottom right), the decrease in [Pu] with addition of sulfate is correlated to a strong decrease in the fraction of PuO$_2$ NPs. Specifically, only 50% of the Pu in solution at 0.05 M sulfate is present as PuO$_2$ NPs, with a significant contribution of mononuclear Pu^{IV} in the form of the sulfate complex. With increasing sulfate concentration, the [Pu] in the solution decreases further, likely due to the precipitation of Pu(SO$_4$)$_2$. The observed yellow precipitate in the samples is currently awaiting characterization by PXRD and Raman. With precipitation of this solid, the fraction of PuO$_2$ NPs that remains in solution increases to ∼80% of the ∼1 mM Pu in solution above 0.5 M sulfate.

Ligand Association at Alkaline pH. Additionally, we studied interactions of the inorganic and organic ligands at alkaline pH. For that, we reacted coagulated PuO$_2$ NP with electrolytes (see Section 4.1 for details on sample preparation). The spectra of all PuO$_2$ NPs samples studied here show the T_{2g} band at 470 cm^{-1} (Figure 30, right) and no changes in the widths of the band, indicating that the crystalline core of the PuO$_2$ NPs was mostly unaffected by the reaction with the different electrolytes. In the oxalate case, the position of the T_{2g} band is unchanged; however, the intensity of the defect band at 578 cm^{-1} is significantly increased, indicating that the crystalline core of the PuO$_2$ NPs was damaged in the presence of this ligand. However, the oxalate sample is overall very heterogeneous and shows a broad distribution of defect densities (not shown here). Moreover, we analyzed the anion signatures to identify their potential binding to the particle surface (Figure 31). The spectra for the oxalate sample contain no ligand-characteristic bands (not shown), consistent with reports that oxalate adsorbs on metal oxide surface mostly under acidic conditions [35].

In the case of nitrate, the symmetric stretching vibration ($\nu_1(NO_3^-)$) in crystalline NaNO$_3$ is typically found at 1068 cm^{-1} [36] and in aqueous NaNO$_3$ solution at 1050 cm^{-1} [37]. The spectra in Figure 31 show the $\nu_1(NO_3^-)$ band at 1053-1059 cm^{-1}, notably in between the expected band positions of the solid-state and solution species. One interpretation of this intermediate band position is that the nitrate ions are associated with the PuO$_2$ NP surface.

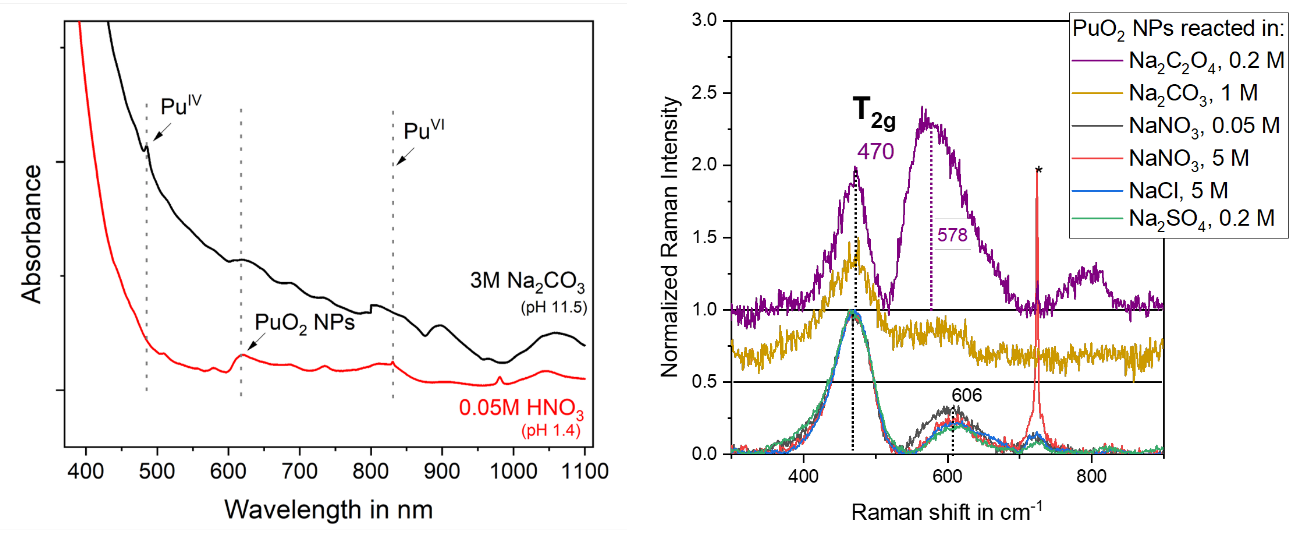

Figure 30. Left: UV visible absorption spectrum of PuO$_2$ NPs in 3 M Na$_2$CO$_3$ (pH 11.5), showing a strong scattering background as well as characteristic PuO$_2$ NP absorption bands, indicating the stability of the PuO$_2$ NPs in solution. No evidence of particle dissolution, i.e., absorption bands of dissolved Pu^{IV} or Pu^{VI}, is found in the spectroscopic data. Right: Solid state Raman spectra of PuO$_2$ NPs reacted with different electrolytes, showing only the T$_{2g}$ region of the spectra. Excitation was done with a 532 nm laser. The asterisk marks a band from co-crystallized NaNO$_3$ at 724 cm-1.

Next, we investigated the interactions between the PuO$_2$ NPs and sulfate that showed strong surface complexation at acidic pH. It was previously reported for selenate, which is isostructural to sulfate, that the adsorption of the ligand on Al oxide surfaces resulted in a shift of $\nu_1(\mathrm{SeO}_4^{2-})$ from 824-827 cm^{-1} in crystalline Na$_2$SeO$_4$[38], to 837 cm^{-1} for dissolved SeO$_4^{2-}$ to 850 cm^{-1} for monodentate inner-sphere adsorbed SeO$_4^{2-}$ on Al oxide [39]. Similar behavior was observed for the sulfate adsorption on Al (hydr)oxides[39], and can therefore be expected for adsorption on the PuO$_2$ NPs as well. The $\nu_1(\mathrm{SeO}_4^{2-})$ band of sulfate in crystalline Na$_2$SO$_4$ is observed at 992 cm^{-1}, so if sulfate was adsorbed on the PuO$_2$ NP surface, a shift to higher wavenumbers by up to 25 cm^{-1} can be expected. As shown exemplarily for three spots (A-C) in Figure 31, left, no such shift or shoulders of the $\nu_1(\mathrm{SO}_4^{2-})$ band are found, indicating that at least under alkaline conditions, interactions between sulfate and and the particle surface are negligible.

Another interesting ligand is carbonate, which was found to stabilize high concentrations of PuO$_2$ NPs in alkaline solutions 4.1. The spectra in Figure 31 show an intense peak at 1070 cm^{-1}. In comparison, carbonate in Na$_2$CO$_3$ has an intense doublet of $\nu_1(\mathrm{CO}_3^{-})$ bands at slightly higher wavenumbers, 1080 and 1079 cm^{-1} [40]. It is noted that a sharp peak at 1068 cm^{-1} could potentially originate from co-crystallization of NaNO$_3$; however, the only other sample that showed this peak was PuO$_2$ NPs reacted in concentrated NaNO$_3$, suggesting that this peak in the carbonate sample is caused by carbonate rather than nitrate. Notably, the band position is consistent with previous reports that assign a vibrational frequency of 1070 cm^{-1} to adsorbed carbonate on electrode surfaces [41]. Therefore, we conclude from the Raman spectra that there is some evidence for a chemical interaction between this ligand and the PuO$_2$ NP surface under alkaline conditions. Additional investigations reacting carbonate with PuO$_2$ NPs synthesized in the absence of nitrate will be conducted to confirm this interpretation.

Moreover, we collected a UV visible absorption spectrum of the PuO$_2$ NP solution containing 3 M Na$_2$CO$_3$ at pH 11.5 (Figure 30, left). The spectrum shows an intense scattering background, indicating the presence of a large number of particles of considerable size, consistent with DLS results (not shown) that indicated a high heterogeneity of the carbonate samples. Absorption bands are found at 485, 619, 688, 733, and 897 nm. The absence of a sharp feature around 831 nm indicates that no Pu^{VI} is formed. The band at 485 nm is significantly shifted from the Pu^{4+} band position, which might indicate the formation of a small amount of Pu^{IV}-carbonate complexes. The remaining bands are consistent with the characteristic PuO$_2$ NP spectrum [16, 17], confirming the presence of PuO$_2$ NPs in carbonate media at high alkalinity. The spectrum shows no significant shifts as observed in the presence of sulfate or for Pu(IV)-silicate colloids [21].

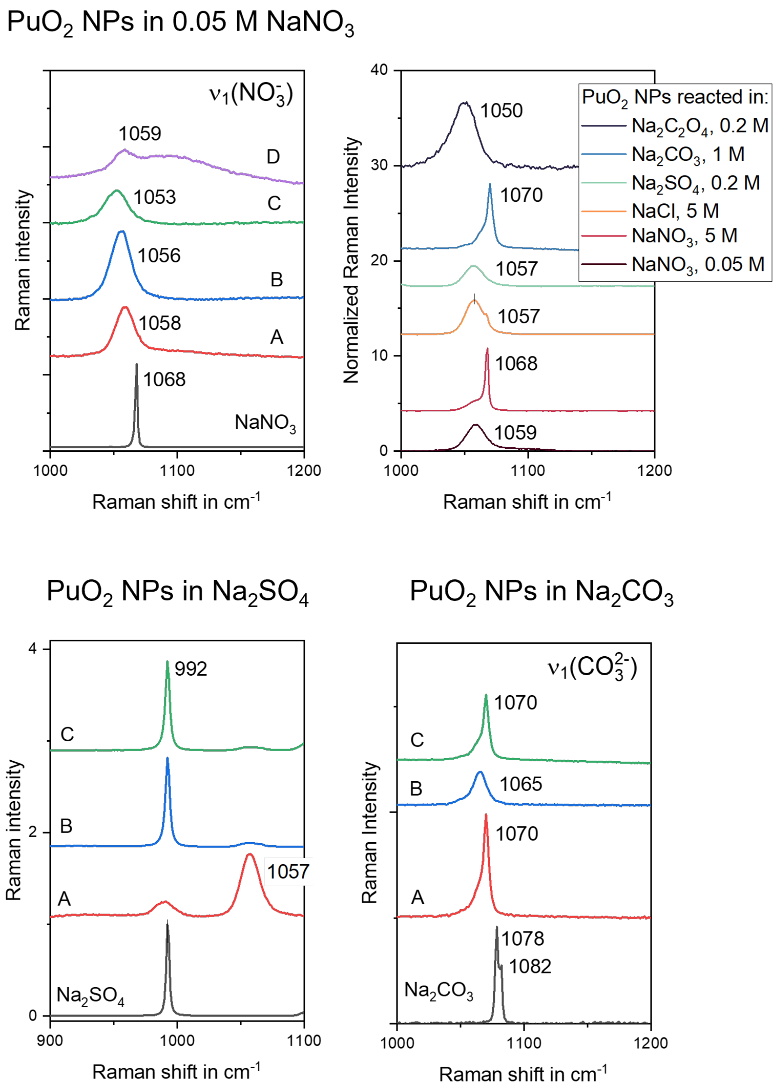
PuO$_2$ NPs in 0.05 M NaNO$_3$

PuO$_2$ NPs in Na$_2$SO$_4$

PuO$_2$ NPs in Na$_2$CO$_3$

Figure 31. Ligand-specific spectral regions of the solid state Raman spectra of PuO$_2$ NPs reacted with NaNO$_3$, Na$_2$SO$_4$, and Na$_2$CO$_3$, allowing insights into the binding of the ions to the particle surface. A-D mark different spots measured on the same sample. Band positions are given in cm^{-1}.

Conclusions. This part of the ongoing project studied the surface interactions of inorganic and organic ligands with PuO$_2$ NPs using absorption and Raman spectroscopy. Ligands such as sulfate, acetate, oxalate, glycine, and trichloroacetic acid were tested under acidic and alkaline conditions. At acidic pH, sulfate and TCA induced particle aggregation and sedimentation, while acetate and glycine showed minimal interactions, which is mainly controlled by the interplay of ligand and surface site (de)protonation. Sulfate exhibited strong surface binding at acidic pH, altering Pu speciation significantly. In contrast, sulfate shows less affinity for the particle surface under alkaline conditions. At high pH values, there is evidence of surface binding of carbonate to the PuO$_2$ NP surface that leads to the stabilization of the particles in solution compared to the carbonate-free system. Other ligands, like the anion of the carboxylic acid oxalate, were shown to have minimal interactions with the particles under alkaline conditions. Overall, the findings highlight the potential for the particle surfaces to bind inorganic and organic ligands, impacting the reactivity of the PuO$_2$ NPs, including their colloidal stability and sorption behavior to solid phases.

5.3 Metal Oxide Single Crystals and Thin Films as Model Systems for Understanding Surface Reactivity using Advanced Spectroscopic and X-ray Scattering Techniques

Ahmet Uysal

Background and Approach. SFG (sum frequency generation) spectroscopy experiments are conducted on ceria thin films, which serve as effective surrogate model system for PuO_2 NP surfaces. We study a range of electrolyte conditions by varying electrolyte concentrations and pH values. These experiments are designed to probe, at the molecular scale, how different anions (such as nitrate, chloride, sulfate, oxalate, and carbonate) interact with the ceria surface and alter the interfacial structure. By collecting SFG spectra in the vibrational regions corresponding to water OH stretching and adsorbed ligand features, we can directly observe changes in the orientation and bonding of interfacial water molecules and surface groups.

Surface orientation and termination control largely the surface reactivity. For instance, the CeO_2 (111) surface has both Ce and O sites exposed each having 1 coordination vacancy. CeO_2 (100), however, has only oxygen atoms at the top surface, with each having 2 coordination vacancies [42]. These differences can significantly affect the ion and water interactions with the surface. Also, these ideal surfaces are likely to change, relax, and undergo surface reconstruction based on the solution conditions. Therefore, in situ observations are required. We will conduct surface X-ray scattering experiments to directly resolve the surface structures under various solution conditions. A beamtime proposal is submitted to the Advanced Photon Source. Thin film ceria substrates will also be used in X-ray measurements for comparison to SFG experiments (Figure 32).

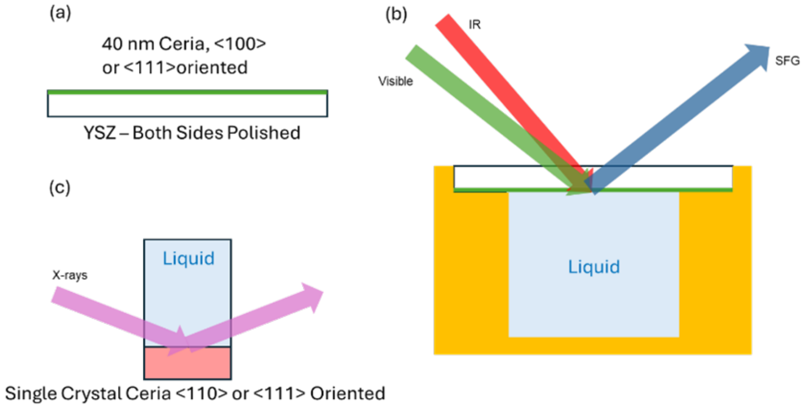

Figure 32. (a) 40 nm ceria thin films on yttrium stabilized zirconia (YSZ) substrates are used for SFG spectroscopy studies. (b) Substrates are placed on the Teflon sample cells in contact with the desired liquid for interfacial studies. The polarization of each laser beam can be controlled to obtain orientation information. S or P polarization combination is reported as SFG, IR, and Visible respectively, like SSP or PPP. (c) Single crystal ceria substrates will be used for surface X-ray scattering experiments.

Preliminary Results. Preliminary SFG studies were conducted on YSZ substrates to develop cleaning procedures and optimize the laser conditions. Cleaning and surface treatment are highly important. Typically, samples are sonicated in water and isopropanol to remove major organic and polar contaminants. Finally, the substrates are treated with ozone to remove smaller contaminants. The SFG measurements are done immediately after the cleaning procedure. Figure 33 shows the -OH region SFG spectra collected under PPP polarization combination at the YSZ water interface. The SFG signal is proportional with the amplitude of the effective second order polarizability of the oscillators. The broad -OH signal is expected from oxide interfaces. The $\sim$3200 cm^{-1} band is typically assigned to strongly hydrogen bonded water populations and $\sim$3500 cm^{-1} band is assigned to weakly hydrogen bonded water populations. The $\sim$3700 cm^{-1} peak corresponds to free -OH vibrations, typically observed at the free air/water interface or hydrophobic surfaces. YSZ (100) surface is terminated with oxygen [43]. Therefore, the dominance of strongly hydrogen bonded -OH signal is expected. However, the sharp free-OH signal is puzzling. It suggests some hydrophobic patches on the surface or surface reconstruction. This peak appears only after cleaning procedure and disappears at aged samples. YSZ (110) surfaces have mixed Zr and O sites that water molecules can coordinate. Overall, weaker hydrogen bonded water molecules dominate this surface.

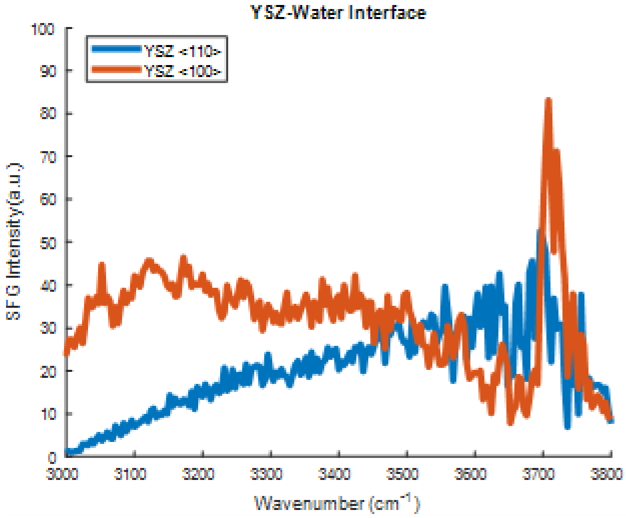

Figure 33. SFG (PPP) spectra collected from YSZ (110)- (blue) and YSZ (100)-water (orange) interfaces.

Figure 34 shows initial measurements of the pH-dependent SFG data at YSZ (100)-liquid interface. With increasing pH, only the intensity of 3500 cm^{-1} band increases while strongly hydrogen bonded band and free OH peak stay relatively unchanged. This suggests that the increasing number of negatively charged sites at high pH orient water molecules toward the surface.

Outlook. We will conduct more detailed pH-dependent studies on ceria surfaces to determine the point of zero charge at different surface terminations and solution conditions and compare them to the nanoparticle studies discussed in detail in Report Section 2.2. We will also conduct surface X-ray scattering experiments with the same substrates to resolve electrolyte interactions with the ceria surface. These investigations, utilizing ceria thin films as model system for PuO_2 NP surfaces, provide molecular-scale insights into ligand association on the particle surface. In addition to the spectroscopic investigations conducted the nanoparticle samples (Section 5.1), these insights offer a deeper understanding of the molecular mechanisms underpinning the colloidal reactivity observed in Section 4.1. This mechanistic understanding is essential for ensuring that advanced thermodynamic modeling efforts accurately reflect realistic chemical reactivity, which is critical for reliable and accurate predictions of the chemical speciation of PuO_2 NPs under varying solution conditions, including those relevant to the Hanford waste tanks.

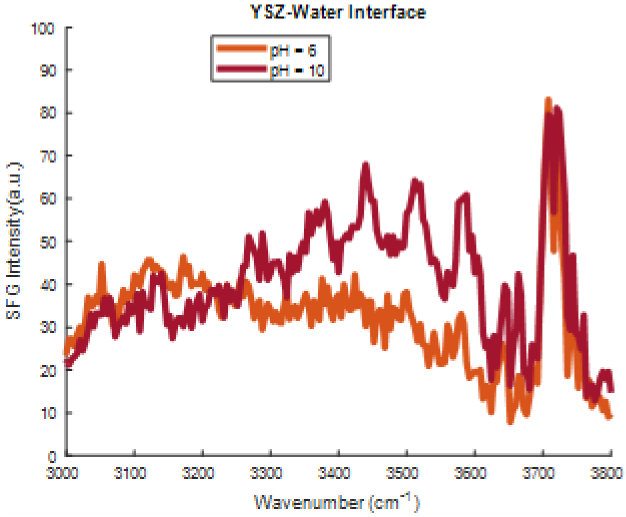

Figure 34. SFG (PPP) spectra collected from liquid YSZ (100) interface at pH 6 (air equilibrated deionized water) (orange) and at pH = 10 (adjusted with NaOH) (red).

6 Partitioning of PuO_2 NPs and Surface-Modified PuO_2 NPs on Crystalline Silico Titanate (CST)

Julia Neumann, Richard E. Wilson

Background. The goal of this part of the project is to experimentally characterize the partitioning of PuO_2 NPs on the ion exchange material used in the tank side cesium removal (TSCR) process, which is crystalline silico titanate (CST, [44], IONSIV R9140-B obtained from Honeywell). Previous laboratory tests of this material, using samples from the Hanford tanks, demonstrated that CST partitioned up to 70 percent of the plutonium and americium contained in the tank supernatants, [3, 45]). However, a systematic characterization in terms of distribution ratios under process-relevant conditions such as high pH, high ionic strength, and the impact of inorganic and organic ligands on the partitioning is currently unavailable. This lack of data poses a risk that plutonium loadings on CST columns discharged from the TSCR process could exceed 100 nCi/g, surpassing the threshold for transuranium (TRU) waste. Such as outcome would result in significant regulatory, financial, and operational challenges. To address this, the goal of this Subtask is to systematically investigate the adsorption of PuO_2 NPs on CST through batch sorption experiments to determine sorption isotherms, including traditional distribution ratios. Additionally, column experiments are conducted to provide process-relevant data for the TSCR process. These experiments will support the development of models describing the partitioning of PuO_2 NPs on CST, enabling control of feed characteristics in the TSCR process, aimed at minimizing the risk of generating TRU waste in the TSCR process. By ensuring that Pu loadings remain below 100 nCi/g CST while maximizing CST's cesium capacity, this approach will allow for a safe and cost-efficient process adaptation without triggering additional regulatory requirements or necessitating extra partitioning steps.

Methods. Preliminary batch sorption experiments were conducted using a PuO_2 NP solution under waste tank relevant conditions (2 M NaNO3, 0.7 M NaOH, referred to as tank simulant, [3]). The solution was prepared by neutralizing a freshly synthesized acidic PuO_2 NPs batch by addition of solid NaOH and $NaNO_3$, followed by equilibration under ambient conditions for 9 days. The supernatant of this solution was used for all sorption experiments, and the resulting [Pu] of 9 μM. CST was prepared according to a PNNL NaOH-washing procedure [4]. Three test series were conducted in this initial stage to cover the impact of (i) pH, (ii) carbonate concentration, (iii) tank waste-relevant metals and ligands on the PuO_2 NP partitioning on the CST. Samples were equilibrated for 1 day and allowed to settle for 3 h before aliquots were taken for radiometric counting to determine the respective distribution ratios.

In addition to the distribution ratios gathered from batch sorption experiments, column experiments give valuable insights into sorption capacity and breakthrough behavior, and display a more realistic scenario in terms of solid to liquid ratios and contact time. Therefore, we conducted some initial tests using self-built columns filled with CST. As feed, we used the same sample solution under tank simulant conditions as used in the batch sorption experiments. In the first experiment, the column consisted of the CST bed (4.5 g) sitting on glass wool to control the flow rate. The column was pre-equilibrated with 100 mL Pu-free simulant, and then a volume of 180 mL of the simulant containing 1.28 mg Pu-242 was run through the column, followed by flushing with 50 mL Pu-free simulant. During the experiment,

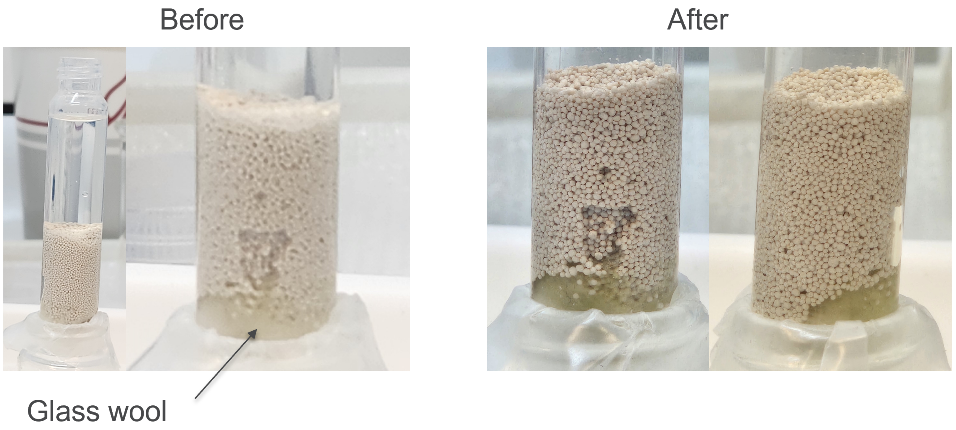

Figure 35. Photographs of CST before and after running 180mL of PuO_2 NP containing Hanford simulant through the columns. The CST sits on glass wool to control the flow rate that turned green during the experiment.

fractions were collected for radiometric counting. Due to dissolution of the glasswool, the column clogged increasingly during the experiment decreasing the flowrate significantly, until further dissolution induced a sudden breakthrough and increase flowrate, at which point the experiment was stopped, and the column flushed with the Pu-free simulant. Figure 35 shows the column before and after the experiment. Clearly, the glass wool changed color from white to green, indicating strong association of the PuO_2 NPs with the glass wool. Therefore, [Pu] measured in the effluent represent adsorption of PuO_2 NPs on CST as well as the glass wool. For direct comparison, a second column without glass wool was tested, running at a somewhat higher flow rate.

Batch Sorption Experiments. The results from the preliminary batch sorption experiments are presented in Figure 36. Strong partitioning of PuO_2 NPs on CST is observed at pH > 8, with Pu concentrations in solution reduced from 9 μM to $\sim$0.25 μM. This corresponds to a removal efficiency of over 97 % under these conditions. As shown in Figure 36 (right), the sorption affinity decreases significantly with increasing carbonate concentration in solution, with the fraction of PuO_2 NPs adsorbed to CST decreasing from approximately 94% to 66%. These values correspond to **102 and 72 ng Pu-242/g CST, or 0.4 and 0.28 nCi/g CST, respectively**.

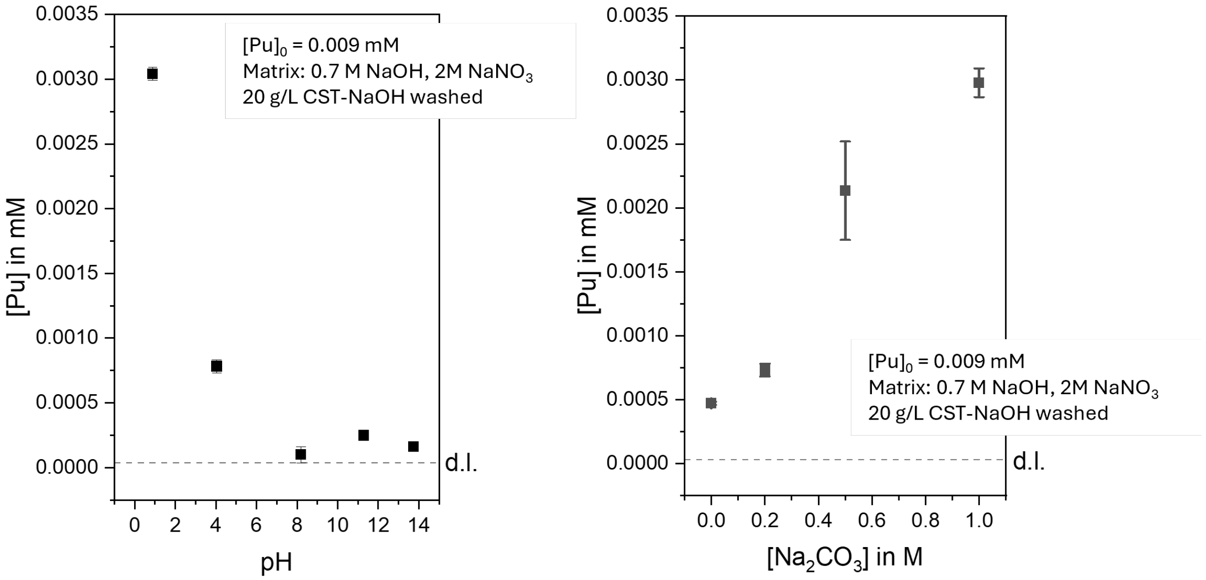

Figure 36. Batch sorption experiments of PuO_2 NPs in 0.7 M NaOH and 2 M $NaNO_3$ on CST as function of pH (left, by addition of HNO_3) and Na_2CO_3 concentration (right). d.l. - detection limit.

In the test series for Hanford-relevant metal ions and ligands, the impact of Ca^{2+}, Al^{3+}, oxalate, and sulfate were evaluated. The initial experiments (Figure 37) indicate a negligible impact of low concentrations of Ca^{2+}, oxalate, and sulfate, as measured Pu concentrations are comparable to values measured in the absence of these additives (approximately 0.5 μM Pu, cf. Figure 36, right). However, at higher concentrations of $CaCl_2$ and $AlCl_3$, the precipitation of $Ca(OH)_2$ and $Al(OH)_3$ resulted in highly efficient removal of PuO_2 NPs from solution, with [Pu] falling below the detection limit of LSC. For the applied LSC procedure, this detection limit was determined to be 0.037 μM Pu-242. These findings highlight the importance of understanding the interplay between solution chemistry and PuO_2 NP partitioning on CST. The observed sensitivity to carbonate concentrations and the potential for enhanced removal via precipitation mechanisms suggest avenues for optimizing the TSCR process to minimize Pu loadings on CST columns.

In Year 2 of the ongoing project, additional extensive series of batch sorption experiments are planned at both ANL and Clemson to develop a comprehensive and robust dataset of PuO_2 NPs sorption isotherms on CST. The experiments will systematically investigate Hanford tank waste-relevant concentrations of $NaNO_3$, OH^- concentrations, and other key solution parameters. Additionally, competitive adsorption studies of Cs^+ and Sr^{2+} will be conducted to evaluate the influence of co-contaminants on Pu partitioning. In parallel, efforts will be made to identify suitable adsorbents for Pu removal prior to the TSCR processs. Common commercial materials such as monosodium titanate (MST), TiO_2, ZrO_2, and Fe_2O_3 will be explored for their potential to efficiently adsorb PuO_2 NPs.

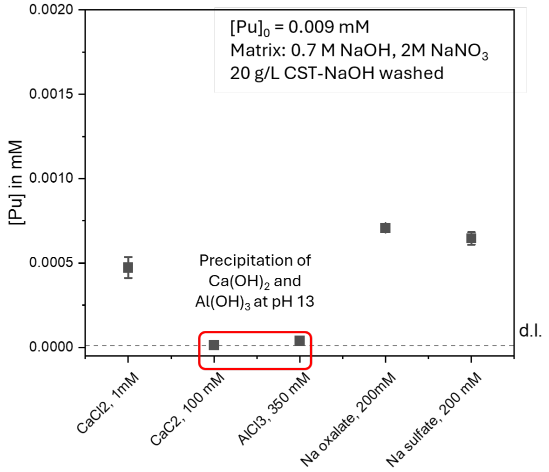

Figure 37. Batch sorption experiments of PuO_2 NPs in 0.7M NaOH and 2M $NaNO_3$ on CST for different metals and organic ligands present in the Hanford tanks. d.l. - detection limit.

Column Experiments. The normalized [Pu] in the effluent, relative to the [Pu] in the feed, for the two tested columns are shown in Figure 38. In the column containing glass wool, the [Pu] in the effluent is initially low, remaining below 20% of the [Pu] in the feed. This is significantly lower than the effluent [Pu] observed in the column without the glass wool, which ranges between 50-80%. These results confirm the visual observation that PuO_2 NPs are strongly retained by the dissolving glass wool, as indicated by its color change from white to green. However, the column without glass wool also exhibits a notable reduction in [Pu] in the effluent, suggesting an inherent affinity of CST for PuO_2 NPs. This finding is consistent with the batch sorption experiments described earlier and with previous tests for Cs removal from Hanford tank waste samples using CST [3]. Importantly, in neither of the two tested columns was the full Pu capacity reached during the experiment, as the [Pu] in the effluent never reached the [Pu] in the feed(i.e., a relative [Pu] of 100 percent, marked by the dashed line in Figure 38. These findings overall indicate that both glass wool and CST contribute to Pu retention, albeit likely through different mechanisms.

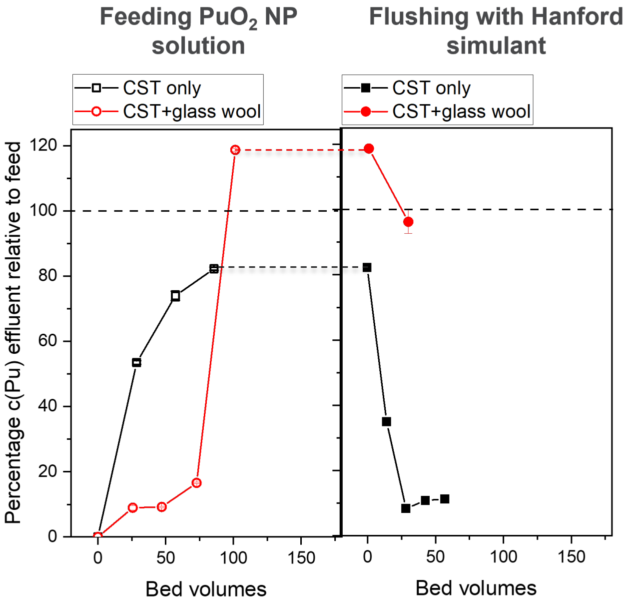

Figure 38. Breakthrough curves of the two column experiments, showing the sorption of PuO_2 NPs by CST (left panel) and the reversibility of this process (right panel).

The column experiment in the absence of glass wool provides a preliminary quantification of the partitioning process of PuO_2 NPs on CST. The total amount of Pu in the feed for this experiment was 0.98 mg. Based on the measured [Pu] in the effluents and the respective volumes of the individual fractions, a total of 0.29 mg Pu-242 is adsorbed onto the CST (4.5 g), corresponding to a **surface coverage of 0.065 mg Pu-242/g CST, or 250 nCi Pu-242/g CST**. To test the reversibility of PuO_2 NP adsorption on CST, the Pu-loaded column was flushed wih 100 mL of Pu-free simulant. As shown in the right panel of Figure 38, the majority of desorption occured within the first 25 bed volumes, after which only small amounts of Pu were recovered from the column. Overall, a total of 0.11 mg Pu-242 were recovered in the flushing phase, corresponding to 36% of the adsorbed Pu. This leaves behind a **residual surface coverage of 0.04 mg Pu-242/g CST, corresponding to 156 nCi/g CST**.

Conclusions and Outlook. These findings highlight the strong retention of PuO_2 NPs by CST, even under dynamic flow conditions, demonstrating that Pu loadings are likely to exceed the regulatory threshold for transuranic (TRU) waste. Notably, these experiments did not reach the full Pu capacity of CST, highlighting the potential for even higher loadings under extended operational conditions. These findings underscore the importance of optimizing CST usage in the TSCR process to minimize regulatory challenges and ensure safe waste management related to undesired Pu partitioning. The observed partial reversibility of Pu sorption indicates that desorption processes may play a role in optimizing CST reuse or disposal strategies. However, the relatively high residual Pu coverage after flushing underscores the need for further investigation into the mechanisms governing Pu retention and desorption.

In Year 2, additional column experiments will be conducted with more controlled flow rates and improved sampling protocols to enhance data quality. These experiments will systematically investigate the impact of salt and hydroxide concentrations, as well as competitive adsorption of Cs^+ and Sr^{2+}, to provide a robust and comprehensive dataset for the modeling team. The ultimate goal is to develop predictive models that enable process adaptations to maintain Pu loadings below the TRU waste threshold while maximizing CST's cesium capacity. The gathered data and insights will be of utmost importance for ensuring safe and cost-efficient process adaptations, minimzing regulatory challenges, and optimizing waste management strategies.

Scientific Communication of Project Results To Date

Publications:

J. Neumann, B.A. Powell, D.A. Montgomery, R.E. Wilson, (2025). Colloidal behavior of plutonium oxide in concentrated electrolyte solutions. Waste Management Symposia 2025: Conference Proceedings, Article ID: 25207. https://www.osti.gov/biblio/2565226

J. Neumann, D.A. Montgomery, B.A. Powell, R.E. Wilson, Synthesis of UO2 nanoparticles via coulometric titration and impact of electrolytes on particle formation and properties, *in preparation*.

S. Nayak, B.A. Powell, J. Neumann, R.E. Wilson, Potentiometric Titrations and Surface Complexation Modeling of An(IV)O2 (An = Ce, Th, Pu): Insights into Nanoparticles and Bulk Materials, *publication planned*.

J. Neumann, B.A. Powell, D.A. Montgomery, R.E. Wilson, 'Reactivity of Plutonium Oxide Nanoparticles in Concentrated Electrolytes: Insights from Light Scattering, Spectroscopic Characterization, and Surface Complexation Modeling', *publication planned*.

Conference Contributions:

J. Neumann, B.A. Powell, D.A. Montgomery, R.E. Wilson - 'Thermodynamic and spectroscopic characterization of plutonium oxide colloids reacted in concentrated electrolyte solutions', Chemistry and Migration Behavior of Actinides and Fission Products in the Geosphere, New Orleans, LA, United States, September 2025.

J. Neumann, B.A. Powell, D.A. Montgomery, R.E. Wilson 'Colloidal behavior of plutonium oxide in concentrated electrolyte solutions', American Chemical Society Spring Meeting, San Diego, CA, United States, March 2025.

J. Neumann, B.A. Powell, D.A. Montgomery, R.E. Wilson 'Colloidal behavior of plutonium oxide in concentrated electrolyte solutions', Waste Management Symposia 2025: Education and Opportunity in Radwaste Management, Phoenix, AZ, United States, March 2025.

References

(1) Delegard, C.; Jones, S. *Chemical Disposition of Plutonium in Hanford Site Tank Wastes*; tech. rep. PNNL-23468 Rev. 1; 2015, DOI: 10.2172/1233488.

(2) Wilson, R. E.; Skanthakumar, S.; Soderholm, L. *Angewandte Chemie International Edition* **2011**, *50*, 11234–11237.

(3) Campbell, E. L.; Westesen, A. M.; Colon, F. C.; Boglaienko, D.; Levitskaia, T. G.; Peterson, R. A. *Separation Science and Technology* **2021**, *56*, 1457–1465.

(4) Campbell, E. L.; Fiskum, S. K.; Peterson, R. A. *Characterization of CST Post-Processing AP-105 Hanford Tank Waste*; tech. rep.; Pacific Northwest National Lab.(PNNL), Richland, WA (United States), 2021.

(5) Bell, J.; Coleman, C.; Costanzo, D.; Biggers, R. *Journal of Inorganic and Nuclear Chemistry* **1973**, *35*, 629–632.

(6) Davis, J. A.; Kent, D. B. *Reviews in Mineralogy and Geochemistry* **1990**, *23*, 177–260.

(7) Sposito, G. *Environmental science & technology* **1998**, *32*, 2815–2819.

(8) Kosmulski, M. *Advances in Colloid and Interface Science* **2020**, *275*, 102064.

(9) Hiemstra, T.; Venema, P.; Van Riemsdijk, W. H. *Journal of colloid and interface science* **1996**, *184*, 680–692.

(10) Cureton, W. F.; Palomares, R. I.; Walters, J.; Tracy, C. L.; Chen, C.-H.; Ewing, R. C.; Baldinozzi, G.; Lian, J.; Trautmann, C.; Lang, M. *Acta Materialia* **2018**, *160*, 47–56.

(11) Knopp, R.; Neck, V.; Kim, J. *Radiochimica Acta* **1999**, *86*, 101–108.

(12) Grenthe, I.; Gaona, X.; Rao, L.; Plyasunov, A.; Runde, W.; Grambow, B.; Konings, R.; Smith, A.; Moore, E.; Ragoussi, M.-E., et al. *Second update on the chemical thermodynamics of uranium, neptunium, plutonium, americium and technetium. Chemical thermodynamics volume 14*; tech. rep.; Organisation for Economic Co-Operation and Development, 2020.

(13) Neck, V.; Altmaier, M.; Seibert, A.; Yun, J.-I.; Marquardt, C. M.; Fanghänel, T. *Radiochimica Acta* **2007**, *95*, 193–207.

(14) Parkhurst, D. L.; Appelo, C., et al. *US geological survey techniques and methods* **2013**, *6*, 497.

(15) Hobart, D.; Morris, D.; Palmer, P.; Newton, T. *Formation, characterization, and stability of plutonium (IV) colloid; A progress report*; tech. rep.; Los Alamos National Laboratory (LANL), Los Alamos, NM (United States), 1989.

(16) Ockenden, D.; Welch, G. *Journal of the Chemical Society (Resumed)* **1956**, 3358–3363.

(17) Micheau, C.; Virot, M.; Dourdain, S.; Dumas, T.; Menut, D.; Solari, P. L.; Venault, L.; Diat, O.; Moisy, P.; Nikitenko, S. I. *Environmental Science: Nano* **2020**, *7*, 2252–2266.

(18) Abdel-Fattah, A. I.; Zhou, D.; Boukhalfa, H.; Tarimala, S.; Ware, S. D.; Keller, A. A. *Environmental science & technology* **2013**, *47*, 5626–5634.

(19) Walther, C.; Cho, H.; Marquardt, C. M.; Neck, V.; Seibert, A.; Yun, J.-I.; Fanghänel, T. *Radiochimica Acta* **2007**, *95*, 7–16.

(20) Walther, C.; Rothe, J.; Brendebach, B.; Fuss, M.; Altmaier, M.; Marquardt, C. M.; Büchner, S.; Cho, H.-R.; Yun, J.-I.; Seibert, A. *Radiochimica Acta* **2009**, *97*, 199–207.

(21) Estevenon, P.; Dumas, T.; Solari, P. L.; Welcomme, E.; Szenknect, S.; Mesbah, A.; Kvashnina, K. O.; Moisy, P.; Poinssot, C.; Dacheux, N. *Dalton Transactions* **2021**, *50*, 12528–12536.

(22) Wilson, R. E.; Hu, Y.-J.; Nitsche, H. *Radiochimica Acta* **2005**, *93*, 203–206.

(23) Cohen, D. *Journal of Inorganic and Nuclear Chemistry* **1961**, *18*, 211–218.

(24) Runde, W.; Reilly, S.; Neu, M. *Geochimica et cosmochimica acta* **1999**, *63*, 3443–3449.

(25) Kim, S.-Y.; Asakura, T.; Morita, Y. *Journal of Radioanalytical and Nuclear Chemistry* **2013**, *295*, 937–942.

(26) Veirs, D. K.; Smith, C. A.; Berg, J. M.; Zwick, B. D.; Marsh, S. F.; Allen, P.; Conradson, S. D. *Journal of alloys and compounds* **1994**, *213*, 328–332.

(27) Lee, M.; Park, Y.; Kim, W. *Journal of Radioanalytical and Nuclear Chemistry* **2007**, *273*, 375–382.

(28) Sarsfield, M. J.; Taylor, R. J.; Puxley, C.; Steele, H. M. *Journal of Nuclear Materials* **2012**, *427*, 333–342.

(29) Hattori, T.; Kobayashi, K.; Ozawa, M. *Japanese Journal of Applied Physics* **2016**, *56*, 01AE06.

(30) Kamali, K.; Ananthasivan, K.; Ravindran, T.; Kumar, D. S. *Journal of Nuclear Materials* **2017**, *493*, 77–83.

(31) Özkan, E.; Cop, P.; Benfer, F.; Hofmann, A.; Votsmeier, M.; Guerra, J. M.; Giar, M.; Heiliger, C.; Over, H.; Smarsly, B. M. *The Journal of Physical Chemistry C* **2020**, *124*, 8736–8748.

(32) Filtschew, A.; Hofmann, K.; Hess, C. *The Journal of Physical Chemistry C* **2016**, *120*, 6694–6703.

(33) Villa-Aleman, E.; Houk, A. L.; Shehee, T. C.; Bridges, N. J. *Journal of Nuclear Materials* **2021**, *551*, 152969.

(34) Knope, K. E.; Soderholm, L. *Inorganic Chemistry* **2013**, *52*, 6770–6772.

(35) Lee, N.; Schuck, P. J.; Nico, P. S.; Gilbert, B. *The journal of physical chemistry letters* **2015**, *6*, 970–974.

(36) Rousseau, D.; Miller, R.; Leroi, G. *The Journal of Chemical Physics* **1968**, *48*, 3409–3413.

(37) Rusli, I.; Schrader, G.; Larson, M. *Journal of crystal growth* **1989**, *97*, 345–351.

(38) Baran, J.; Lis, T.; Marchewka, M.; Ratajczak, H. *Journal of molecular structure* **1991**, *250*, 13–45.

(39) Wijnja, H.; Schulthess, C. P. *Journal of Colloid and Interface Science* **2000**, *229*, 286–297.

(40) Brooker, M.; Bates, J. B. *The Journal of Chemical Physics* **1971**, *54*, 4788–4796.

(41) Moradzaman, M.; Mul, G. *ChemElectroChem* **2021**, *8*, 1478–1485.

(42) Mullins, D. R. *Surface Science Reports* **2015**, *70*, 42–85.

(43) Adhikari, N. M.; Hou, B.; Allen, H. C. *The Journal of Chemical Physics* **2024**, *161*.

(44) Miller, J. E.; Brown, N. E. *Development and properties of crystalline silicotitanate (CST) ion exchangers for radioactive waste applications*; tech. rep.; Sandia National Lab.(SNL-NM), Albuquerque, NM (United States), 1997.

(45) Rovira, A. M.; Fiskum, S. K.; Colburn, H. A.; Allred, J. R.; Smoot, M. R.; Peterson, R. A.; Colisi, K. *Separation Science and Technology* **2019**, *54*, 1942–1951.

Argonne
NATIONAL LABORATORY